Scientific Research Publishing

Atmospheric and Climate Sciences, 2025, 15(1), 72-105
https://www.scirp.org/journal/acs
ISSN Online: 2160-0422
ISSN Print: 2160-0414

Links of Terrestrial Environment with Solar Activity and Solar and Planetary Orbital Motion

Valentina V. Zharkova[1,2], Irina Vasilieva[2,3]

[1]Department of MPEE, Faculty of Engineering and Environment, University of Northumbria, Newcastle upon Tyne, UK
[2]ZVS Research Enterprise Ltd., London, UK
[3]Department of Solar Physics, Main Astronomical Observatory, Kyiv, Ukraine
Email: valentina.zharkova@northumbria.ac.uk, valja46@gmail.com

How to cite this paper: Zharkova, V.V. and Vasilieva, I. (2025) Links of Terrestrial Environment with Solar Activity and Solar and Planetary Orbital Motion. *Atmospheric and Climate Sciences*, **15**, 72-105.
https://doi.org/10.4236/acs.2025.151004

Received: November 6, 2024
Accepted: January 4, 2025
Published: January 7, 2025

Abstract

In this paper we emphasize statistical links between solar activity and orbital motion with various terrestrial phenomena: terrestrial temperature, sea levels, ice areas, frequencies of volcanic eruptions, and Oceanic Nino Index (ONI). *Solar activity links.* The solar activity indices are expressed through the averaged sunspot numbers SSN and the summary curve of eigen vectors of the solar background magnetic field (SBMF). The terrestrial temperature (GLB dataset), global sea level, and volcanic eruption frequencies are shown from the wavelet analysis to have a clear link to the SBMF index, which has the same significant period of 21.4 years. The ice and snow areas in the Northern hemisphere are found to vary with a period of 10.7 years equal to the usual sunspot activity cycle while in the Southern hemispheres, no links to solar activity are detected. *Solar orbital motion links.* The variations of total solar irradiance (TSI) measured from the abundance of ^{14}C isotope during the Holocene are shown to have a similar period of 2200-2300 years (Hallstatt's cycle) as the solar inertial motion (SIM) induced by the gravitation of large planets, In the current millennium the amount of TSI deposited on Earth in the March-September to Northern hemisphere is ≈1.2% higher than in the September to March in the Southern hemisphere. The wavelet analysis of ONI revealed the two significant periods of 4.5 and 12 years. The first one is shown to have a link to the lunar perigee period variations while the second period is linked to the Jupiter period of revolution about the Sun whose gravitation seems to trigger terrestrial tectonic processes leading to volcanic eruptions. The ONI variation is noticeably linked to the occurrence of underwater volcanic eruptions (correlation of 25%), which, in turn, are linked to the tidal forces of Jupiter, the Moon and the Sun in its inertial motion. Joint effects of the solar activity and the solar and planetary orbital motion are likely to govern the current changes in the terrestrial environment defining continuing climate change.

Keywords

Terrestrial Temperature, Terrestrial Sea Level, Terrestrial Ice Areas, El Nino Southern Oscillation, Volcanic Eruptions, Underwater Volcanic Eruptions, Solar Magnetic Field, Solar Activity, Solar Inertial Motion, Correlation, Jupiter Revolution Period, Lunar Perigee Period

1. Introduction

The global terrestrial temperature was shown to rise in general, from 1850 and at an unprecedented pace after the 1970s by 1.4C, in total [1]-[3] that imposed many concerns among researchers and humankind as a whole. A few main external forcing mechanisms are used in the Coupled Model Inter-comparison Project (CMIP) models: solar activity, volcanic eruptions and longer term linear trends (to represent the anthropogenic CO_2), however to what extent they are accurate remains to be established yet. The abrupt hike in the terrestrial temperature, coincided with the unusual climate patterns observed globally (Monsoon) [4] as well as regionally (Indian Summer Monsoon (ISM): [4]-[6]. ONI, or El Nino and Southern Oscillations (ENSO) [7] [8], North Atlantic Oscillation (NAO) [9].

There are two types of ENSO, based on spatial patterns of sea surface temperature (SST) around tropical Pacific have been detected: a) one type with a dominated by variability around East Pacific (EP), known as Canonical ENSO or EP type and b) the other type defined by dominated by variability around Central Pacific (CP), known as Modoki or CP type [4] [5] [7].

Different mechanisms of ONI/ENSO formation were considered (see [10] [11] and references therein) Yu 2007, Roy 2018: for CP ENSO, its phase transition (barrier, onset, etc.) happens in the spring and it is phase locked with the season; while for EP ENSO, though it is mainly regulated by the thermocline shifting, the phase shift and barrier varies decade to decade. For extratropical connections for CP ENSO, two mechanisms have been proposed: Equatorial Ocean Advection Theory [12] (Kug *et al.* 2009) and Extratropical Forcing Theory [12] [13]. Following the first theory, anomalous SST along the equatorial Pacific is grown by the Zonal Ocean Advection, while the second theory suggests that it is initially excited by forcing from extra-tropics and then developed by the advection from the tropical ocean.

Recent arguments about what is causing the terrestrial temperature increase in the past centuries and the insistence by IPCC and AGW supporters that it is a product of anthropogenic-induced global warming caused by green house gasses came out with a few essential omissions ignoring important natural effects. The main effect of these effects is the influence of our only star—the Sun—as the only source supplying energy to all planets of the solar system. The Sun is the primary source of energy for the climate of the Earth and other planets. How the terrestrial environment responds to the variations of solar activity and its orbital position is

not clearly understood yet. Plus, the important secondary effects of cosmic rays and clouds are ignored despite their inclusion, which is likely to lead to more realistic scenarios of how the Sun governs the Earth's climate through its effects on the terrestrial environment.

The solar radiation magnitude deposited to Earth is considered affected by solar activity itself, as is the change in Sun-Earth distances caused by solar inertial motion induced by the gravitation of large planets [14] [15]. The solar activity indices are expressed through averaged sunspot numbers [16] and the summary curve of eigen vectors of the solar background magnetic field (SBMF) [17]. Recently, it has been shown that solar activity can also be described by eigenvectors of the solar background magnetic field (SBMF) derived with the principle component analysis (PCA) from the full-disk solar magnetograms of the Wilcox Solar Observatory, US [17]. The modulus of the summary curve of the two principal components of SBMF fits rather closely with the averaged sunspot numbers, which are currently used as the solar activity index [17]-[19].

The advantage of the new proxy of solar activity, the summary curve of two PCs, is in the fact that it not only provides the amplitudes and shapes of solar activity cycles but also gives the leading magnetic polarities. It was also shown that by adding the other eigen vectors of SBMF e.g., produced by quadruple and sextuple magnetic sources, besides the two largest PCs associated with magnetic dipoles, it can replicate closer not only the sunspot index [19] but also shows the closest link to the soft X-ray flux index associated with solar flares [18].

Solar activity was shown to be defined by the solar dynamo action in the two layers of the solar interior, producing two magnetic waves that have close but not equal periods of about 11 years [17]. The interference of these two magnetic waves leads to a grand period in their amplitude oscillations of about 330 - 380 years when the amplitudes are dropped during the grand solar minima (GSM) caused by the wave's beating effect [17]. Such grand periods are separated by GSMs whose timing coincides with the well-known solar minima such as the Maunder minimum (MM), Wolf's, Oort's, Homeric and other grand minima [20]. In fact, similar to the previous GSM, the Maunder Minimum, in 2020 the Sun was entered into the period of a modern GSM lasting until 2053 [17] [21].

During the most recent grand solar minimum (GSM), Maunder Minimum, MM, there was a noticeable reduction in solar radiation by about 3 W/m^2 [22] and, as a consequence, in the average terrestrial temperature which dropped by about 1C [23]. This, in turn, was proxied by the absence of sunspots and active regions on the solar surface during the MM [20]. Although, the terrestrial temperature was found increasing since the Maunder minimum by 0.5C per century [1] [24]. However, from cycle 21, solar activity systematically decreased, which coincided with a decrease in the solar background magnetic field in the approach to the modern grand solar minimum (GSM) [17] [18].

At the same time, in the past few hundred years the Sun has been providing some additional radiation to the Earth because of moving closer towards the

Earth's orbit at the spring equinox location caused by the solar inertial motion (SIM) induced by gravitation of the large planets [14] [15] [25] [26]. These increases in solar radiation are caused by periodic variations of the Sun-Earth distance to, occur every 2100-2300 years, so-called Hallstatt's cycles, which were independently derived from the isotope abundances in the terrestrial biomass [27] [28]. In the current Hallstatt's millennial cycle, the Sun-Earth distances are decreasing from the MM until 2600 which will lead to a continuous increase of solar irradiance deposited to the atmosphere of the Earth (and other planets) [15] [26].

This SIM effect is shown to contribute to the terrestrial atmosphere heating [15] [26], in addition to any heating considered in the terrestrial models. However, the most notable effect of SBMF in the next few decades will come from a reduction of solar activity, or from the modern grand solar minimum (GSM), which started in 2020 and will last until 2053 [17] [21].

On the one hand, any warming due to increased solar activity in 11-year cycles is not considered to be uniform [29], either within the atmosphere or at the ocean surface. On the other hand, the patterns and amplitudes of the derived responses in temperature and ocean levels, are still the subject of some uncertainty. A large response was found in the Pacific in boreal winter: a positive anomaly in the Bay of Alaska [30], and also a reduction in a sea level near the date line at around 20 - 40 N latitudes with a positive anomaly south of the equator, which was interpreted as a strengthening of the SE trade winds crossing the equator, driving increased ocean upwelling and cooler equatorial temperatures [31].

Zharkova and Vasilieva [25] summarised the links between solar radiation and various terrestrial phenomena, like terrestrial temperature, sea levels, ice areas, frequencies of volcanic eruptions, and Oceanic Nino Index (ONI) in both hemispheres. The Oceanic Niño Index (ONI) is found to have a strong (>87%) correlation with the Global Land-Ocean Temperature. The GLB dataset of the terrestrial temperature and global sea level are shown from wavelet analysis [25] to have a significant period of 21.4 years which is clearly associated with the variations in solar activity defined by the summary curve of the largest eigen vectors of the SBMF.

A dominant 21.4-year period is also reported in the variations of the volcanic eruptions in the past 3 centuries also associated with the summary curve of SBMF correlating with the coefficient r = 87%. There is no indication of a noticeable seal level increase [26]. Although, the ice and snow areas in the Southern hemisphere do not show any links to solar activity periods while in the Northern hemisphere the ice area reveals a period of 10.7 years equal to a usual sunspot solar activity cycle [16].

Naturally, there is a spatial variability of tropical Pacific Sea Surface Temperature (SST) leading to different forms of ONI, especially, Central Pacific (CP) ONI, which is the most important one. It is mainly dominated by the variability of SST around CP region [32]. For CP ONI, atmospheric forcing plays the dominant role and it has an extratropical connection [33] over the periods a few century in the

past [34].

Many authors have studied the effects of ice area variations on the changes of the sea level based on a wide range of approaches and methods ([see, for example, [35] [36] and references therein). Although none of these predictions could correctly reflect the precise interaction of the ocean and atmosphere, possibly, because the variations of ice areas are not related directly to the ocean models [37]. The estimations of the current loss of mass for the shores of Amudsen (ices of Pine-Island, Twaits, Smith, Pope and Kohler glaciers vary from 1.4 to 2.9 cm per century [38]-[40]. The glacier Pine Island, which is the most variable one could lead to the increase of the sea level by 3.5 - 10 mm during the next 20 years [41]-[43].

The sea level increases owing to melting ice and snow occurring on the Earth, melting ice of Arctics and Antarctica, and thermal expansion of the water during its warming in the summer [44]. In this sense, the increase in the sea level is a direct consequence of the temperature increase [45] [46]. In particular, Rahmsforrt (2007) [45] developed a semi-empirical approximation for a connection between the temperature and sea level variations in the 20th century that was later explored in a number of papers [47]-[50].

On the other hand, the total solar irradiance (TSI) calculated from the Sun-Earth distances in March-August of every year of the last few centuries is found to grow with every year because the Sun moves closer to the Earth's orbit owing to the gravitation of large planets called solar inertial motion (SIM) while following the measured terrestrial temperature closely. The SIM imposes a period of 2200-2300 years (Hallstatt's cycle) in TSI oscillations which is detected in the Holocene data of solar irradiance measured from the abundance of ^{14}C isotope and confirmed with baseline variations of the SBMF.

The amount of TSI deposited on Earth in 2020 during the spring-winter in the Northern hemisphere is nearly 2% higher than that deposited in the autumn and winter. This trend will continue in the next five centuries until 2600 showing that he amount of TSI deposited between the spring and autumn equinox constitutes 50.103% of overall TSI while between the autumn and spring equinox constitutes 49.897% of the TSI. The additional TSI deposition to the Northern hemisphere is likely caused by SIM's securing of the additional energy input and exchange between the ocean and atmosphere in the terrestrial environment that was recently observed.

Explosive volcanos are another form of natural contribution that has an enormous impact on the climate of the Earth, which involves the troposphere as well as the stratosphere [51]. The role of explosive volcanos shows a noticeable influence on the modelled ENSO [52]. It was also suggested that explosive volcanos during the El Niño phase contribute to its duration, whereas the same during La Niña shortens the period counteracting its duration.

There is an ongoing debate on the causality and correlation between terrestrial temperature increase and the growth of CO_2 and other greenhouse gas concentrations in the terrestrial atmosphere [3]. Although, the recent studies by different

authors (see, for example, [11] [23] [53] and references therein) addressed the role of natural factors (the sun and volcanic eruptions) compared to that from CO_2-led anthropogenic contributions. Furthermore, [11] identifies that the dominance of Central Pacific (CP) ONI and associated with ONI and volcanic eruptions water vapour feedback during that period does play an important role in affecting the terrestrial temperature that confirms the suggestions by Salby (2012) [53].

The possible mechanism could be initiated via a preferential alignment of North Atlantic Oscillation (NAO) phase, generated by explosive volcanos. Recently, [54] have shown that the causal relationship between an increase of the terrestrial temperature and a growth of the CO_2 abundances clearly indicates that the CO_2 presence must be a consequence of the terrestrial temperature growth and not vice versa as assumed by the modern temperature models [3]. This leaves the question still open about major causes of the observed temperature variations on the Earth in a short (decades) and long (millennia) terms. The majority of current climate models may be oversimplified and could benefit from further exploration of the observations presented in the current paper.

The aim of the current study is to demonstrate that solar activity and orbital effects of the Sun and other planets of the solar system on the terrestrial environment can significantly affect the variations of the terrestrial temperature, sea level, volcanic eruptions and formation of El Nino/La Nina and Southern Oscillations defining natural periodic changes of the climate on Earth.

2. Links to Solar Activity Indices

2.1. Wavelet Analysis

Wavelet transform of signals is the spectral analysis method providing a two-dimensional scan of the analysed signal (time and frequency, or period), in which the coordinates of the time and frequency are independent variables [55]. This representation allows one to explore the properties of the signal simultaneously in time and frequency domains. This makes the wavelet analysis an excellent tool for examining the series with time-varying frequency characteristics [55]. By considering the time series in the frequency-time space it is possible to derive dominant periods and their variations in time. The mother wavelet was selected as the Morlet wavelet (the real part of it is damped function of cosine), because with this choice one can obtain a high frequency resolution, which is important for our task.

The power of the wavelet spectra is shown in plots with wavelets by a colour bar plotted next to the wavelet spectrum. The Cone of Influence (COI) marked in the wavelet spectrum by the black dashed line, defines the parts of the spectrum with the essential border effects in the starting and finishing parts of the time series, because of a limited statistical data (boarder effects). Consequently, the results outside the COI are excluded from the further investigation, particularly, in the calculations of the global wavelet spectrum shown by the black curves on the right hand side from the wavelet spectra where we present by the solid black lines the global wavelet spectra integrated over time. The black dashed lines in the global

wavelet plots presents 95% confidence interval for the global wavelet spectrum.

2.2. The Sea Levels and GLB Temperature Variations

2.2.1. General GLB Temperature and Sea Level Variations

The temperature series reasonably complying with these conditions is the series of the surface temperature (GISSTEMP) produced by the NASA Goddard Institute of Space Science (GISS)
https://data.giss.nasa.gov/gistemp/tabledata_v4/GLB.Ts+dSST.txt
accessed 12/06/2023 [56]. This set starts from 1880 and we will name it as GLB hereafter.

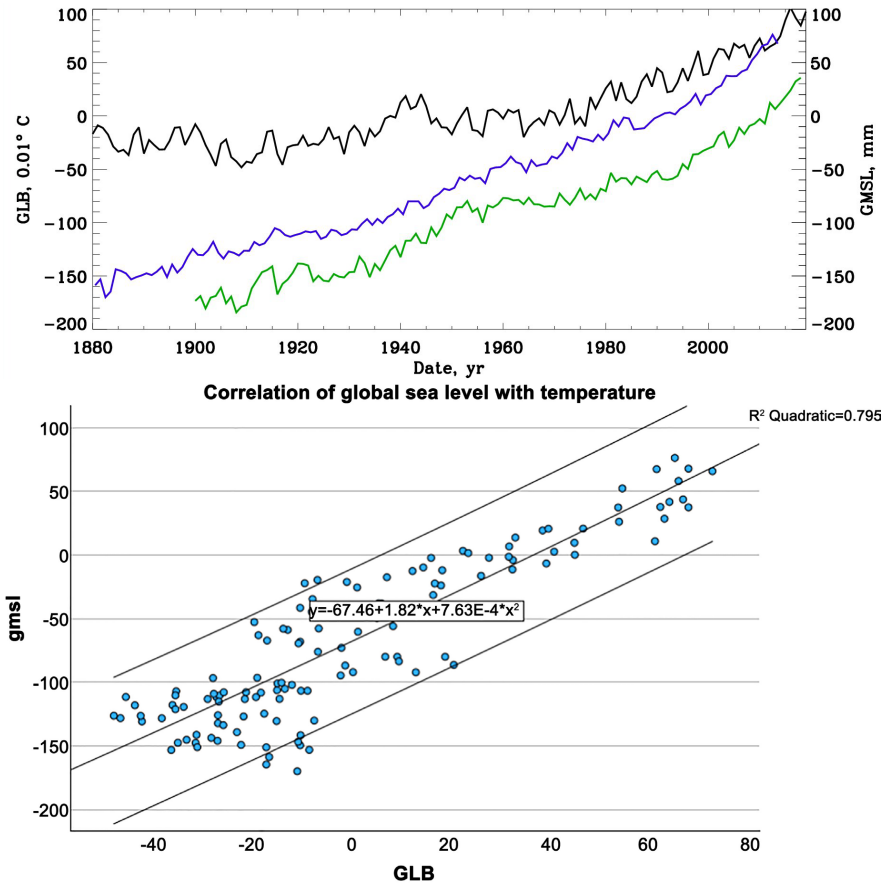

Figure 1. Top plot: The series of the GMSL sea level (blue line) and another sea level data v (green curve) versus the GLB terrestrial temperature (black line) variations. Bottom plot: scatter plot of correlation of the GMSL sea level with the GLB terrestrial temperature, correlation coefficient r = 89%.

The GLB temperature variations are shown in Figure 1 by the black line. The series of temporal variations of the global mean sea level (GMSL) during 1880-2014 (the navy curve) was obtained from the Centre for Protection of the Environment of the USA and SCIRO (Centre for Scientific and Industrial Research Organisation) (http://www.cmar.csiro.au/sealevel/sl_data_mar.html. The green curve represents the sea level variations reported in [57], which reveals the same trend

of the sea level as the blue curve, although showing the differences in the absolute seas levels between two datasets approaching up to 73 mm.

The evaluation shows that the sea level is increased by 195 mm during the period from 1870 until 2004 with an averaged speed of growth of 1.7 ± 0.3 mm/year [58]. Although, according to [59], the growth speed of the sea level was 1.7± 0.9 mm/year that led to the global increase of the sea level by 9.2 cm. The sea level variations show close similarity, in average, to the temporal variations of the GLB variations that confirms findings of the previous studies [45]-[50].

2.2.2. Spectral Features of the Temperature Variations

In order to evaluate the spectral properties of the series and to derive the key periods let us apply the Morlet wavelet analysis to the GLB temperature with the results presented in **Figure 2**.

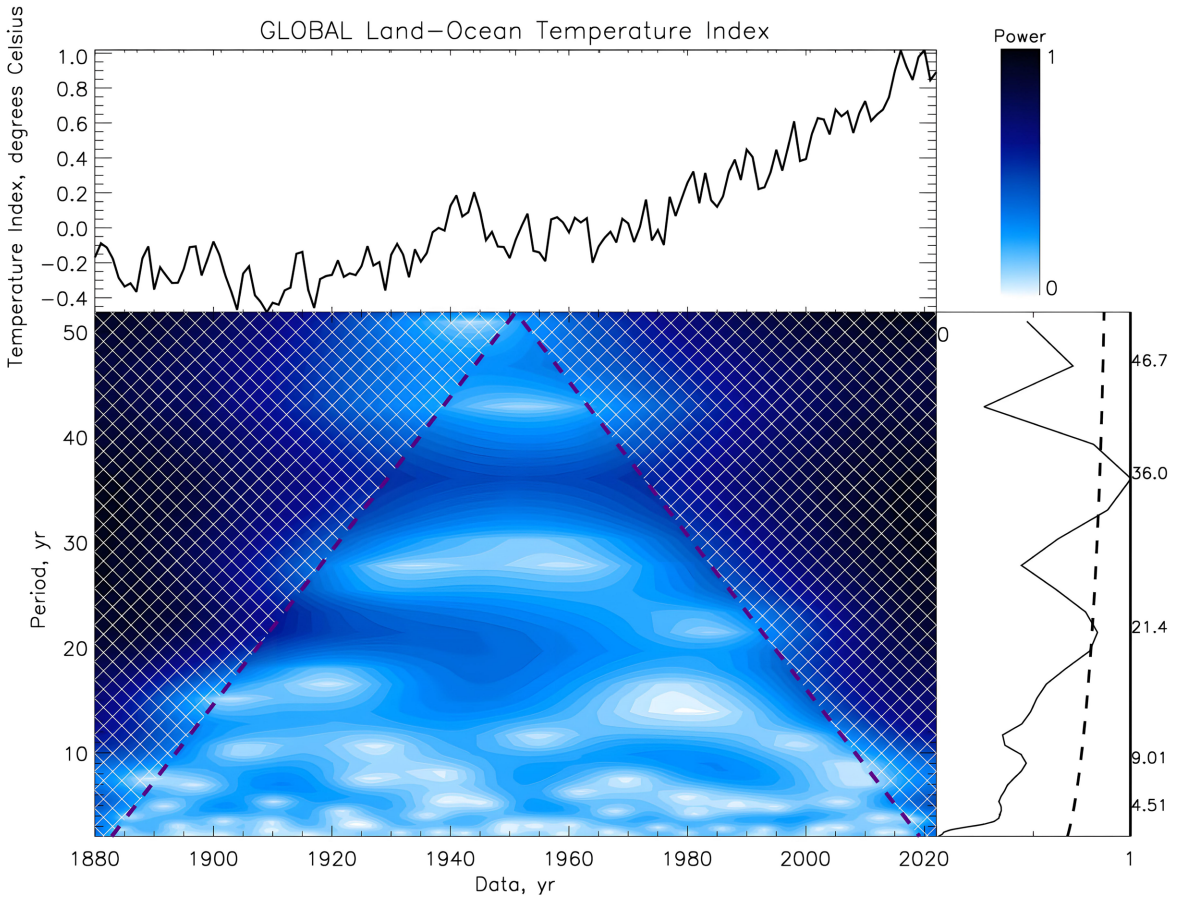

Figure 2. The GLB terrestrial temperature variations (top left plot), the wavelet spectrum of temperature (bottom left plot) with the wavelet power marked by the colour bar (top right plot) and the global (integrated) wavelet spectrum is shown by the black solid line) while the 95% confidence interval marked by the black dashed line.

The most important feature derived from the GLB series of terrestrial temperature is a presence of the statistically significant periods of 21.4 and 36 years. The first period of 21.4 years is corresponding to the oscillation period of a solar magnetic activity cycle derived in the summary curve of eigen vectors of the SBMF

[19] [25] [26].

The period of 36.0 years in the wavelet spectrum of the GLB temperature can be linked to effects induced by some local events, e.g. monsoons, oscillations of El Nino/La Nina indices or other features, which need to be investigated.

2.3. Ice and Snow Areas in the Northern and Southern Hemispheres

The datasets containing the ice and snow areas in the northern and southern hemispheres including Arctic and Antarctica is taken from the National Snow and Ice Data Center) from 1979 until 2022 accessed on 31/07/2023. https://masie_web.apps.nsidc.org/pub/DATASETS/NOAA/G02135/seaice_analysis/. A comparison of the aggregate areas of the ice and snow cover for both hemispheres (blue curve) with the world sea level ((black curve) is shown in **Figure 3** (top plot) showing a direct comparison of the curves. The scatter plots of the correlations of the ice areas with GLB temperature in both hemispheres are shown in **Figure 3** (bottom plot) revealing the similar correlation coefficients r = −0.59 for the both hemispheres.

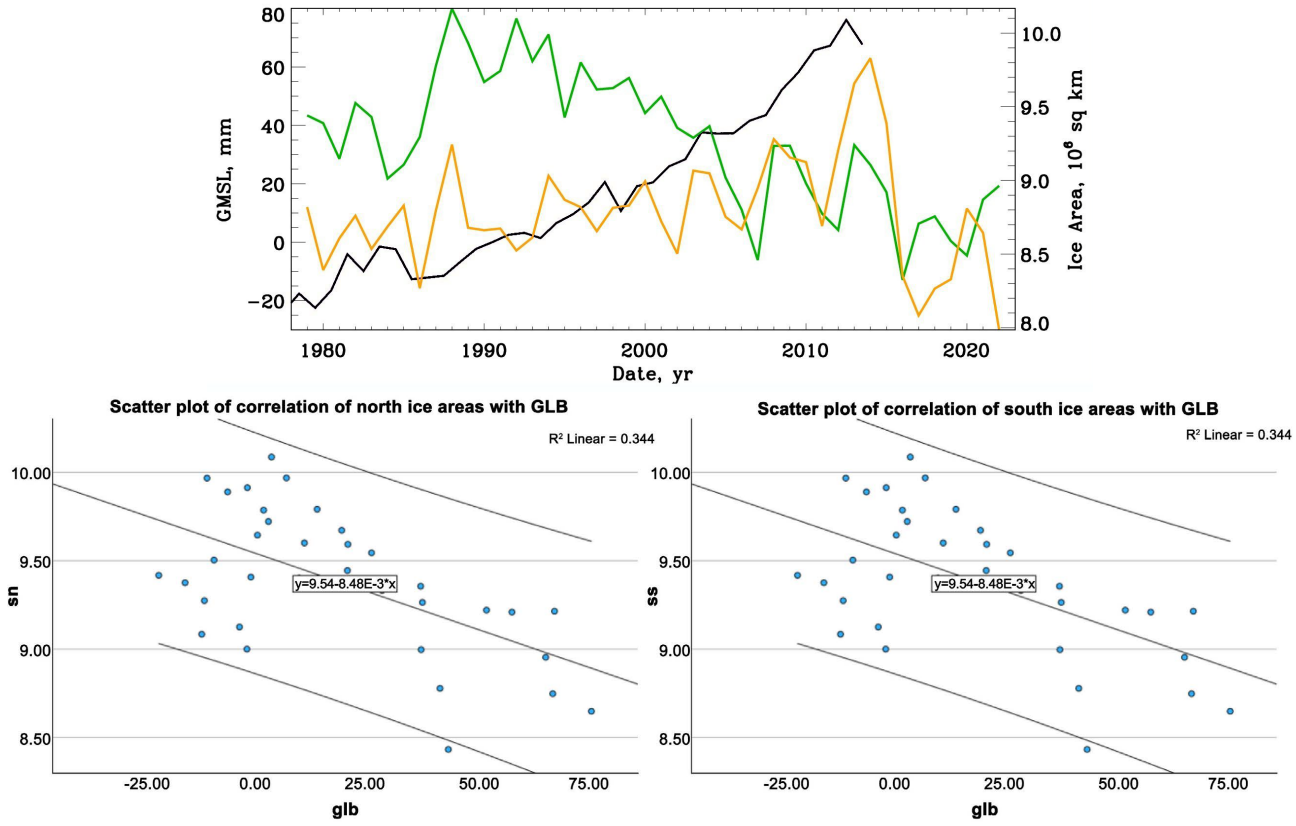

Figure 3. Top plot: The variations of the GMSL of the world ocean (black curve) versus the ice areas of the Northern (green line) and Southern (orange line) hemispheres. Bottom plot: scatter plots of correlation of the GMSL temperature with the ice areas of the Northern (left plot) and Southern (right plot) hemispheres, the correlation coefficient for both r = −59%.

By looking at the plots **Figure 3** (top plot), it becomes evident that the weather patterns seem to have a very different effect in the Northern and Southern

hemispheres. If in the Northern hemisphere the ice areas are steadily decreasing after 1985, while the sea level is increasing, the average area covered by ice in the Southern hemisphere remains the same while showing some oscillations and even ice area increase in 2012-2015 followed by a sharp decrease after 2022. The increase of the sea levels in each hemispheres is linked to a decrease of the ice areas is noticeably linked to a reduction of ice areas in both hemispheres shown in the scatter plots of **Figure 3** (bottom plot).

The wavelet analysis of ice area coverage in Arctic shows (**Figure 4**) for the Arctic ice (top plot) and Antarctica ice (bottom plot). It can be observed that the Arctic and Antarctic ice areas indicate the periods of 4.9 and 5.4 years, respectively. While only Arctics ice areas reveal a confident period of 10.7 years that is the averaged period of solar activity defined by the averaged sunspot numbers [25] [26].

While Antarctica's ice areas do not reveal this link with the solar activity showing some periods of 5.4 and 15.6 years within the 95% confidence level, possibly, affected by some local events. Curiously, this clear period of 5.6 years which can be linked to a solar activity period reported recently [61] [62] and interpreted as an important part of defining a solar cycle shape and power. This could reflect the times close to the minima of solar activity when the ice areas are growing.

Hence, a very interesting feature is detected that the ice and snow areas in the Southern hemisphere were growing until approximately 2013 without any links to solar periods [26] while in the Northern hemisphere there are observed periodic decreases of the ice areas from 1986 occurring with a period of 10.7 years that is the period for a usual solar activity cycle defined by sunspots [19].

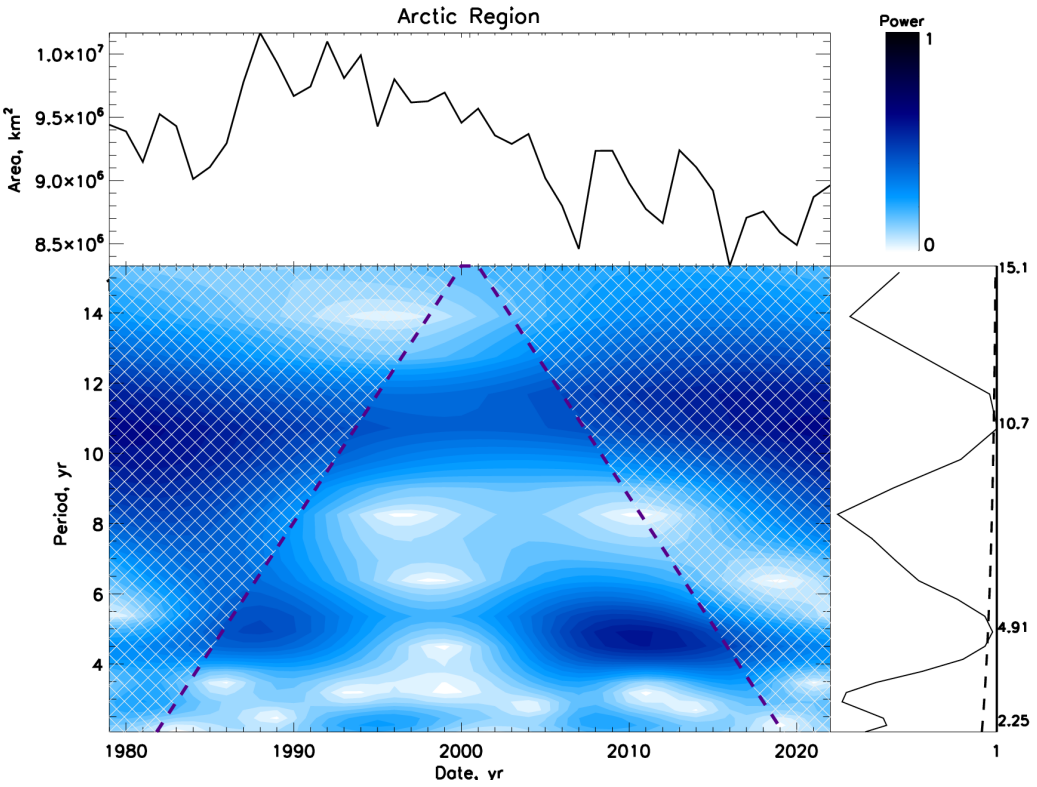

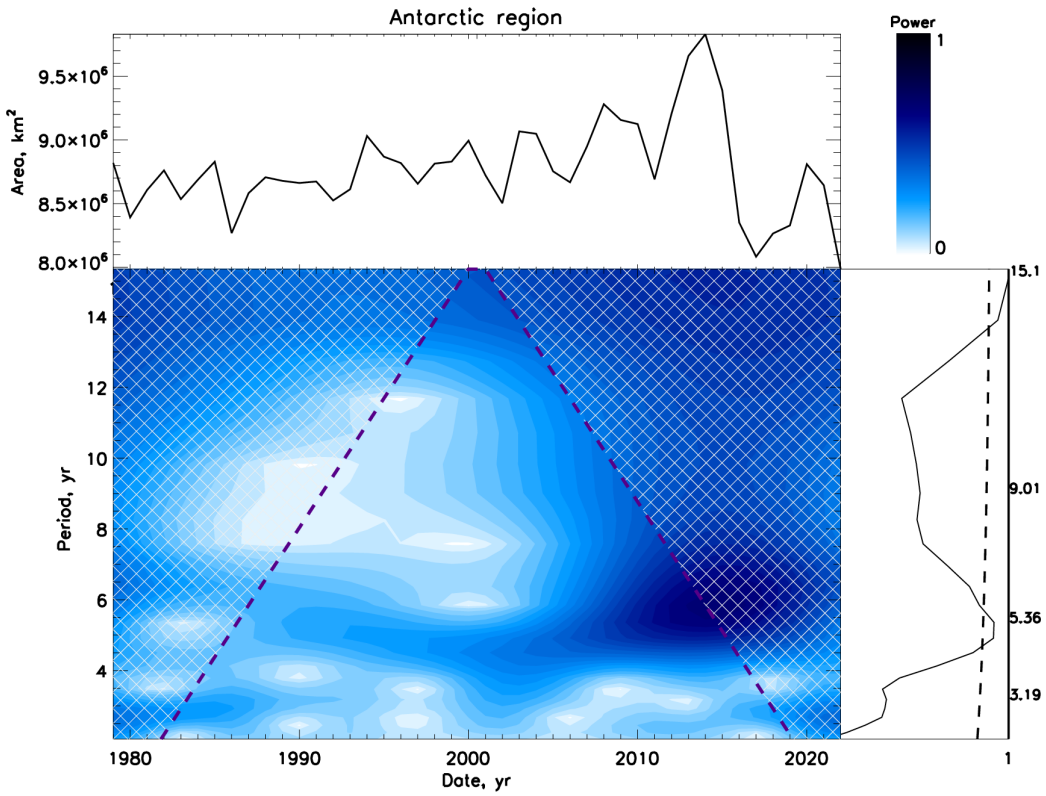

Figure 4. The wavelet spectra of the ice areas in Arctics (top plot) and Antarctica (bottom plot). The global wavelet spectra (black solid line), of ice areas are shown on the right hand side from the wavelet spectra, while the 95% confidence interval is shown by the black dashed line.

Also there was an absence of correlation between the variations of the world ocean level (**Figure 3**, top plot, black curve) and the variations of the summary ice cover areas in the Northern plus Southern hemispheres (blue curve). This can be understood in terms that only the polar ice cups were considered excluding the ice and snow cover on the continents.

Links of the Ocean Level and Ice Area Variations to Solar Activity

In this section we explore the links between the variations of solar activity and solar background magnetic field. and the world sea level (**Figure 5**, top plot), the aggravated (total) ice areas in both hemispheres (**Figure 5**, bottom plot) and terrestrial temperature variations occurred in the past two centuries.

It can be observed that there is clearly present a dominant 21.4 years period of variations of the world sea level shown in **Figure 5**, top plot and not so recognisable tendency of the temperature variations with the sunspot index of solar activity of 11 years [26]. The de-trended curve of a total ice areas in the both hemispheres shown in **Figure 5**, bottom plot confirm a general trend of the correlation of the sea level increases in the 11 years cycles when the summary curve of SBMF has a Southern magnetic polarity and a decrease of the ice areas when the summary curve has a Northern polarity.

The visible agreement between the periods of the sea level curves and the eigen vectors in the summary curve of SBMF closely resonates with the similar correlation detected in the link between the eigen vectors of SBMF and the frequency of volcanic eruptions [60] (see Section 2.4).

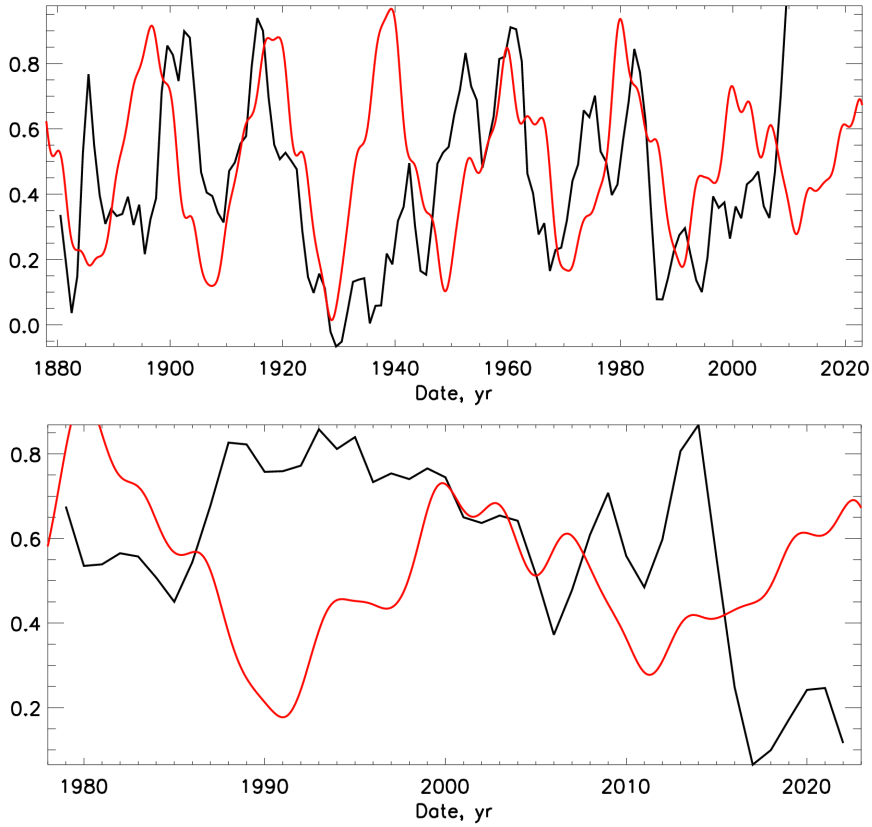

Figure 5. Top plot—The variations of the level of the world ocean level (black line) versus the summary curve of SBMF (red curve). Bottom plot—The variations of the de-trended total ice areas in both hemispheres (black curve) versus the summary of the SBMF (red curve) (see the text for details) (dimensionless units referred to the maximum, black line).

2.4. Links of the Frequencies of Volcanic Eruptions with the Summary Curve of SBMF

Following the technique presented by Vasiljeva and Zharkova [60] a comparison of the normalised summary curve of eigen vectors (EV) and the frequencies of volcanic eruption (VE) plotted in **Figure 6**: top plot, for real EV of SBMF and VE and bottom plot, for the inverted EV, curve EV1, multiplied by minus unity. The inversion of EV is done so that the maxima of EV1 correspond to the EV cycles with southern polarity and coincide with maxima in VEs, while the minima of VEs correspond to the EV cycles with the northern polarity.

The Spearman correlation analysis of the overall VE and EV1, the inverted EV data, was carried out using the IBM SPSS Statistics package (v28) for a) the whole interval from 1750 until 2020, b) for the early interval 1750-1868 and c) for the later interval 1868-1950 & 1990-2020 [60]. The correlation for the whole interval

of the datasets VE and EV1 (1750-2020) produced a positive correlation coefficient of 0.21. This low correlation between VE and EV1 is likely to be affected by the problems with the datasets reported for the periods before 1868 and between 1950-1990 [60].

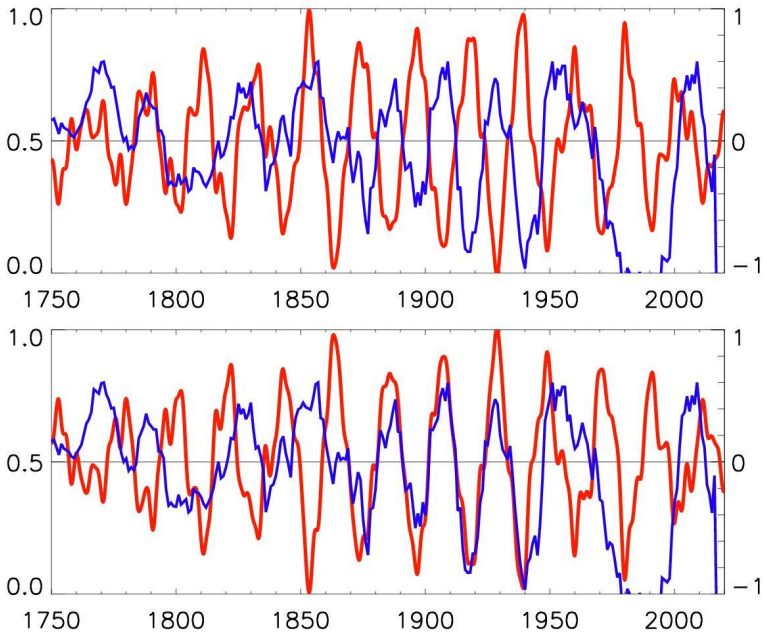

Figure 6. Top plot: The averaged normalised (dimensionless units) number of volcanic eruptions (VEs) (blue curve) (the left Y-axis), versus the summary curve of eigen vectors (EV) of the solar background magnetic field [17] (red curve) normalised by its maximum (the right Y-axis). Positive magnitudes of the summary curve correspond to the northern polarity and negative ones to the southern polarity of SBMF. Bottom plot: the volcanic eruption (VE) numbers (left Y-axis, blue line) versus the inverted summary curve of eigen vectors (EV1) (the right Y-axis, red line) with positive magnitudes corresponding to southern polarity and negative to the northern one. For the correlation coefficients between these two curves see the text and the scatter plots in **Figure 7**. A courtesy of Vasilieva and Zharkova [60].

For the period b) of volcanic eruption in 1750-1868 the correlation coefficient of VEs with EV1, or the inverted EVs, was −0.33, while for the volcanic eruptions in the period c) of 1868-1950 & 1990-2020 the correlation reaches the high magnitude of 0.84. Definitely, tn the period c) from 1868 onwards (excluding 1950-1990 with open nuclear testing) there is a strong correlation of 0.84 of volcanic eruptions VEs with EVs of the solar magnetic field when it has the southern polarity. This defines a strong correlation of VEs with the summary curve of EVs having southern polarity and minima at EVs with EVs with northern polarity.

The correlation results are also checked with the scatter plots for the key two periods b) and c) shown in **Figure 7** for 1750-1868 (top plot) and for 1868-1950 & 1990-2020. The scatter plots were fit with linear and quadratic functions which seem to be rather close. The standard deviations (STDs) from the fits are shown by the inner set of lines about the fits, and the confidence intervals for a 95%

confidence level are shown by the outer lines. The results reveal very close correlation coefficient of 0,84 in the second period (1868-1950) and much more scattered one (−0.325) in the first period (1750-1868).

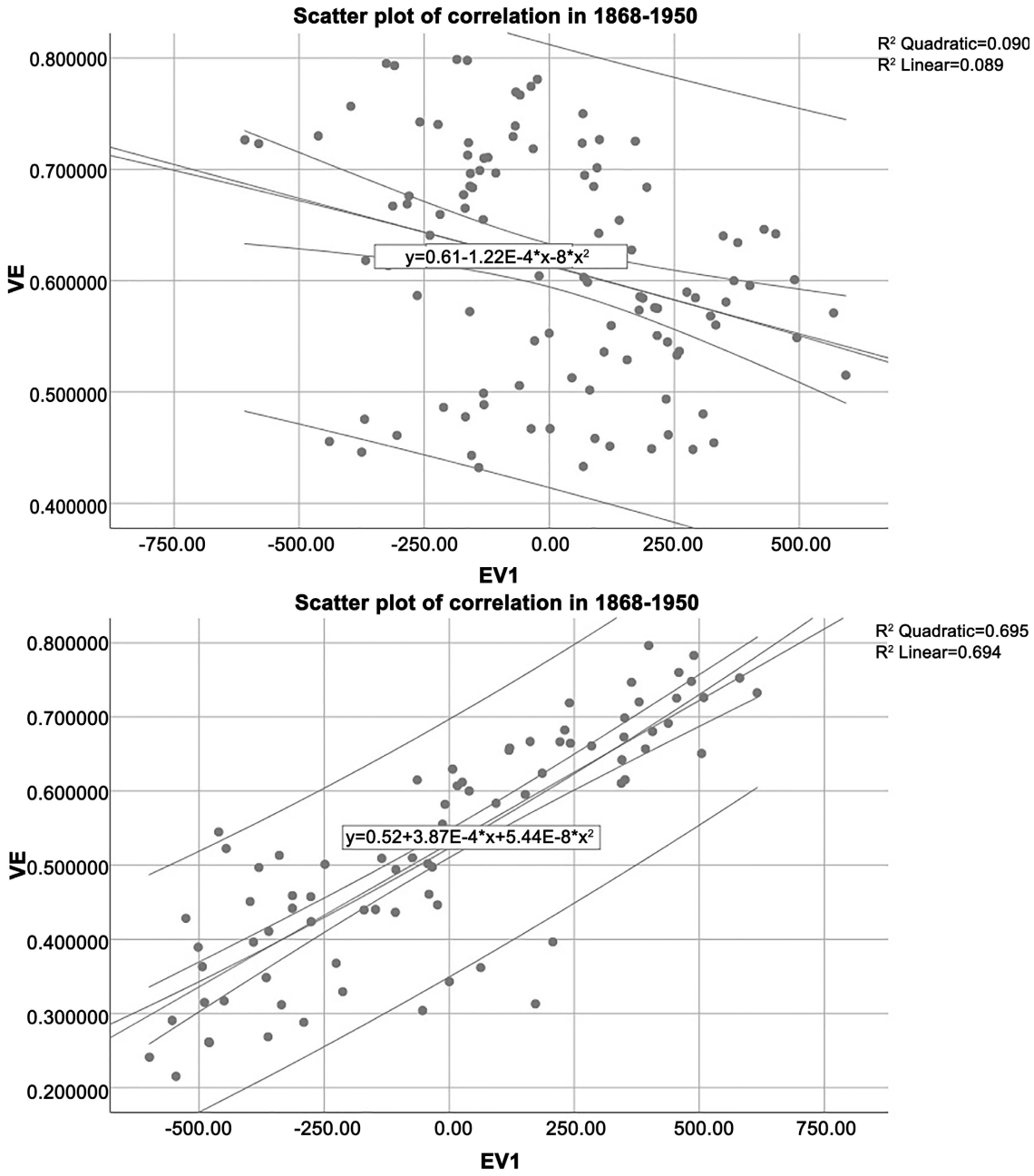

Figure 7. Top plot: A scatter plot of correlation of the normalised volcanic eruption (VE) frequency with the inverted summary curve of eigen vectors (EV1) of SBMF for the data from 1750-1868 with Spearman correlation coefficient of −0.325. Bottom plot: The scatter plot of the correlation of VE frequency with the inverted summary curve of eigen vectors (EV1) for 1868-1950 with Spearman correlation coefficient of 0.840. This defines a strong correlation of VEs with the summary curve of EVs having southern polarity and minima at EVs with EVs with northern polarity. The central lines provide the best linear and quadratic fits (with formula) of correlation coefficients, the near lines define standard deviations of the fits and the outer lines show the 95% confidence intervals for the derived correlation. A courtesy of Vasilieva and Zharkova [60].

Hence, the volcanic eruption (VE) frequencies have maxima every 21.4 years occurring during the periods when the summary curves of eigen vectors (EVs) have the southern polarity. This coincides with the period of 21.4 years found from the volcanic eruption frequencies with the wavelet analysis using the Morlet wavelet [60].

The finding confirms that the maximum volcanic eruptions occur during the maxima of the even solar activity cycles with the summary curve of EVs of SBMF have southern magnetic polarity. Furthermore, this link between VEs and EVs can also explains not only the short term periods of 10.7/21.4 years of volcanic eruptions. Although, a. longer period of 350 years was previously detected in the volcanic eruptions frequency [63], which coincides with the grand solar cycle period ranging in 330 - 380 years detected in the EVs of SBMF [17] [18].

Therefore, similarly to the variations of the ice areas mentioned in Section 2.3, there is a strong correlation of 0.84 of the frequencies of volcanic eruptions in 1868-1950 and solar magnetic cycles with the southern magnetic polarity of the summary curve of two eigen vectors of the SBMF. This can be understood in terms of the accepted views that the increase of geomagnetic disturbances often correspond to an increase in the interplanetary magnetic field of the southern polarity (see, for example, [64]-[69]).

3. Links to Solar and Planetary Orbital Motion

3.1. Links of the Terrestrial Temperature and Solar Irradiance Induced by Solar Inertial Motion

Solar inertial motion is a rotation of the Sun about the barycentre of planetary orbits caused by the gravitation of large planets of the solar system (Jupiter, Saturn, Neptune and Uranus) [70]-[72]. The methodology for the calculation of Total Solar Irradiance (TSI) using inverse squares of the distance between the Sun and Earth taken from the official NASA and Paris-Meudon Observatory ephemeris is described in the book chapter by [15], which also provided the plots of solar irradiance variations in the two millennia 600-2600 [15]. The TSI results calculated for the Sun-Earth distances in March-September on years in the past two centuries are plotted above the terrestrial temperature curve as shown in **Figure 8**.

It can be seen that the sum of all TSI in W/m^2 deposited to the Earth daily during the period when the Sun is closest to the Earth's orbit (March-August) grows with every coming year of this millennium because the Sun moves closer and closer to the Earth and other planetary orbits. This is caused by the solar inertial motion, or gravitation of large planets shifting the Sun from the focus of ellipse towards the position oof a spring equinox in the Northern hemisphere. It can be seen that the TSI magnitudes calculated for the spring-summer months when the Sun is closest to the Earth orbit follow rather closely the current temperature trend.

This growth of total solar irradiance during spring and summer months caused by the Sun moving closer to the Earth orbit is evidently reflected in the temperature trend measured by the NASA stations, which seems to miss the temperature

measurements in the same locations during the other months (September-February) when TSI and, consequently, the temperature, drops much lower than expected for a normal Sun's position in the focus of the elliptic orbit of the Earth and other planets. This is a very important finding because of a close correlation of this temperature curve with the ocean level shown in Figure 1 as it indicates that the extra-heating provided by the Sun at the times, when it is closer to the Earth orbit, is consumed by the ocean and is likely to be processed over the next months or years.

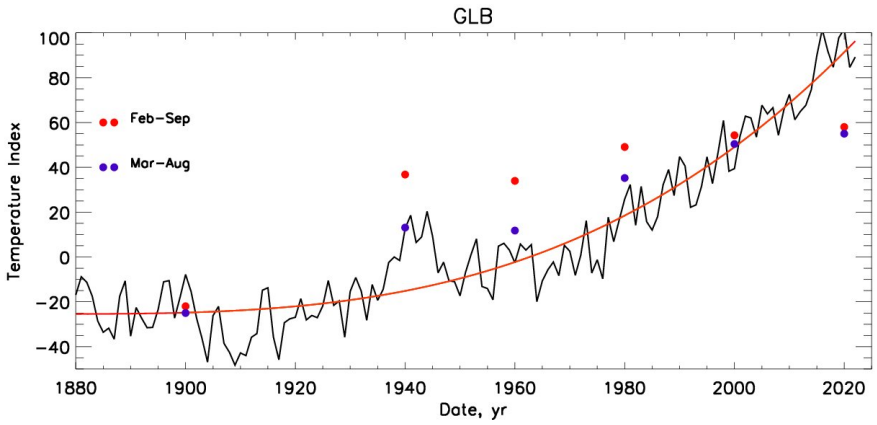

Figure 8. The terrestrial temperature variations (black line) and averaged temperature (red line) versus the total solar irradiance (TSI) of the Sun affected by SIM in the spring-summer months as per the legend on the plot. The solar irradiance is calculated by adding the daily irradiance for given spring-summer months in the Northern hemisphere when the Sun is closest to the Earth's orbit [15].

The fact that the land-ocean temperature measured correlates with the spring-summer TSI magnitudes, which is not considered when producing the solar forcing for the terrestrial temperature models [3] is likely to create the discrepancy between the solar heating function used in the current temperature models. Besides any increases of the terrestrial temperature caused by the change of temperature measurement techniques, e.g. surface or two meters above, urban conditions or in country side where the first points produce by default a higher temperature [73] [74], there is additional solar heating caused by solar orbital motion induced by the gravitation of large planets.

In the other words, the steady solar heating function applied in the IPCC models uses the TSI magnitudes averaged over the annual Earth orbit while the real temperature measurements they use to interpret are likely to be carried only during the spring-summer periods when the Sun's input is maximal because it is closest to the Earth orbit. What is also important that only the current temperature measurements made in March-September are closely linked to the ocean level as reported above in this study following [26], thus affecting the essential exchange between the ocean-stored CO_2 and the atmosphere temperature and compositions following Henry's law. These points need to be explored in the future temperature

models.

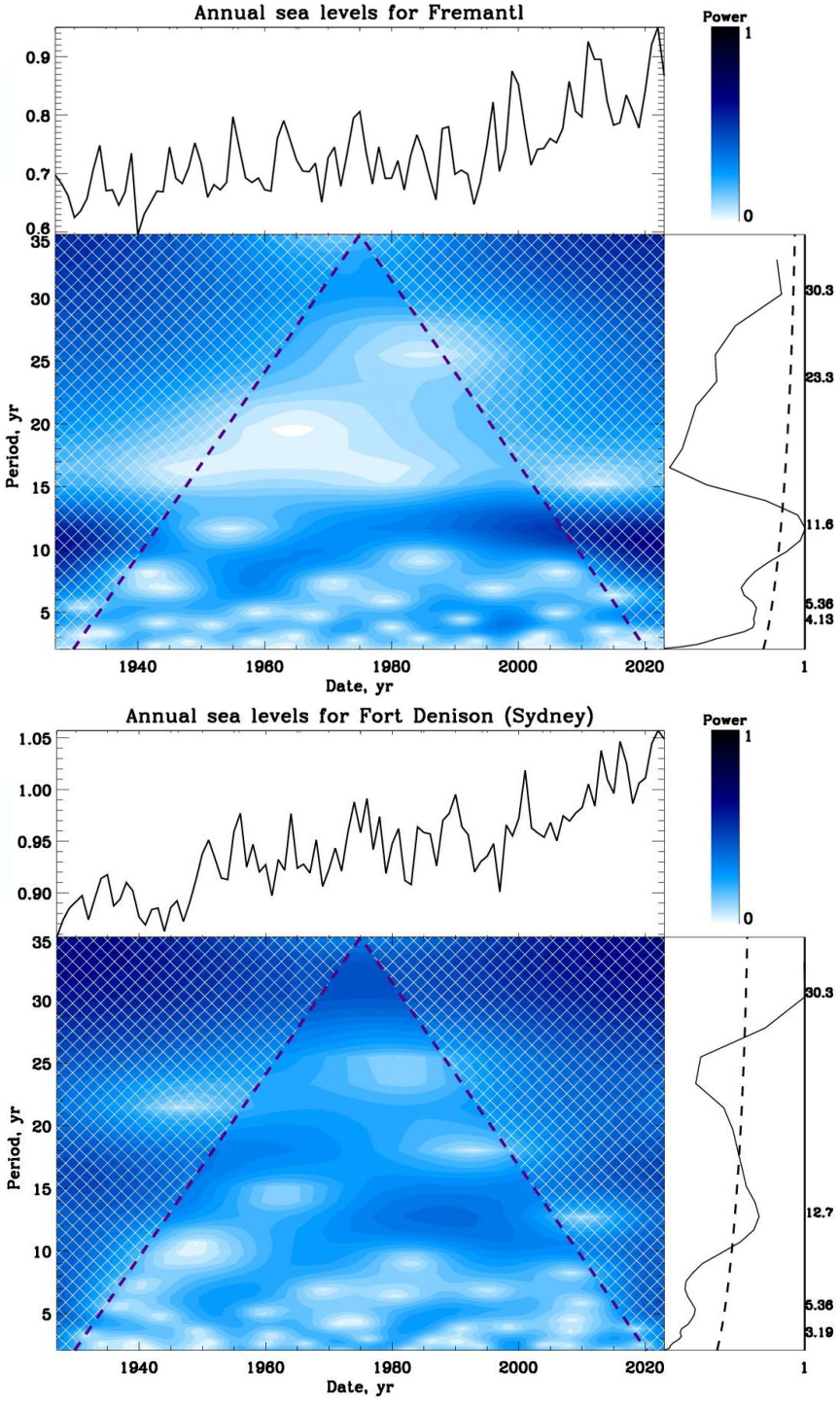

Figure 9. Wavelet spectra of the sea level variations in Fremantle (top plot) and Sydney (bottom plot) bays. In each plot—in the top row there are presented: the original sea level series (left) and the wavelet power colour bar (right); in the bottom row—the wavelet spectra with the Cone of Influence (COI) marked by black dashed line (left) and the global (integrated) wavelet spectra marked by the black solid line and 95% confidence interval marked by the black dashed line (right).

3.2. The Sea Level Variations in the Southern Hemisphere

In order to evaluate the spectral properties of the series of the sea level measured in the Southern hemisphere and to derive the key periods let us apply the Morlet wavelet analysis to the sea level sets at Fremantle (top plot) and Sydney bay (bottom plot) datasets presented in **Figure 9**.

It can be seen that the sea level in Fremantle bay shows a clear period of 11.6 years which appears well above the 95% confidence interval marked by the black dashed line. The sea level in the Fremantle bay area has also clear indication to the period 4.2 - 5.4 years. At the same time, in Sydney bay the sea level there is clear detection above 95% confidence interval of the period of 12.7 ears and some indications of the period of 4.2 - 5.4 years.

Neither of these periods resemble the period of 10.7 years derived for the solar activity by sunspots or for the modulus summary curve derived from the eigen vectors of solar background magnetic field [26]. The cause of these periods of 11.6, 12.7 or 5 years needs to be additionally investigated that will be done in the sections below.

3.3. ONI/ENSO Index Variations

3.3.1. Spectral Features of the ONI/ENSO Inde

The Oceanic Niño Index (ONI) is taken from https://www.climate.gov/news-features/understanding-climate/climate-variability-oceanic-nino-index.

ONI, which also often called as ENSO (El Nino Southern Oscillation), follows the three months measurements of an average temperature of the sea surface in the East-Central tropical part of the Pacific ocean nearby the international line of the date change. These measurements demonstrate the ocean temperature to be colder or warmer than the averaged one over 30 years.

In order to evaluate the spectral properties of the Oceanic Nino Index (ONI) series covering the variations of El Nino/La Nina and Southern Oscillations (ENSO) formed in Pacific and to derive the key periods, let us apply the Morlet wavelet analysis to the temperature sets with the results presented in **Figure 10** for the ONI/ENSO index.

The most important feature derived from this series of the ONI index is a presence of the statistically significant two periods of 3.57 - 5.05 years and 12 years with some tendency to have a double 12 years period restricted by a short length of the ONI data. The lower period of 4 - 5 years in the ONI index variation can be related either to the tectonic plate movements [75], or more likely to the effects of a half cycle of the lunar perigee oscillation of 8.85 years on the elliptical orbit of the Moon leading to stronger tides twice a year when the lunar perigee is aligned with the Earth-Sun axis leading to the semidiurnal lunar tides [76] (see Section 3.3.4). These lunar effects can trigger motion of tectonic plates leading to volcanic eruptions and also linked the local conditions in the ocean through Brewer-Dobson circulation and dominant positive Antarctic Oscillation (AAO) [11].

The most puzzling is the larger period of 12 years in the ONI index, which is

detected with the high accuracy within 95% confidence interval. This period is not clearly linked to any solar activity indices shown in Section 2, which within in the same duration of the data have the period of about 10.7 years [19] [26]. Hence, this 12 year period of the ONI index oscillation is outside the standard effects of solar activity as was also clearly shown in the previous Section 2. The latter period is linked to the revolution of Jupiter as discussed in Section 3.3.3.

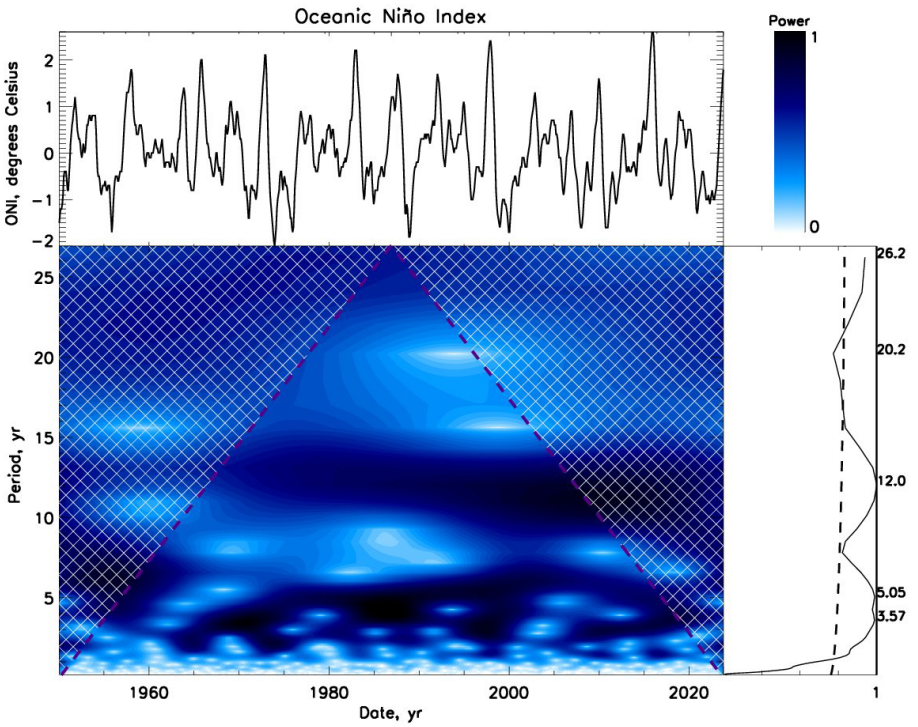

Figure 10. Top plot: The wavelet spectra of the ONI index revealing the distinguished periods of 4.5 and 12 years with the measured ONI/ENSO variations (top left), the colour bar of the wavelet power (top right), the wavelet spectrum with the Cone of Influence (COI) marked by the dashed line (bottom left) and the global (integrated) wavelet spectrum (black solid line) with the 95% confidence interval (black dashed line).

3.3.2. Links of the ONI Index with the Frequencies of Volcanic Eruptions

In this section we do not consider various local terrestrial factors considered to contribute to the ONI/ENSO occurrences as discussed in the introduction. Instead, we attempt to investigate a role on the planet Earth of the tidal forces induced by the planet Jupiter in the positions where the largest number of volcanic eruptions occur.

This period of 12 years appearing in the ONI oscillations can come from the Jupiter revolution about the Sun and tidal forces to Earth associated with the positions of Jupiter with respect to Earth [77].

Most likely, this tidal link should occur via volcanic eruptions in the ONI/ENSO areas, which can affect the occurrences of El Nino/La Nina events and Southern Oscillation and the terrestrial and ocean temperature. In reality, the most contribution comes from the under-water (submarine) volcanic eruptions as suggested

by a few authors [7] [75]. Hence we consider both the surface and under-water volcanic eruptions in the ONI/ENSO area as shown in Figure 11 [77].

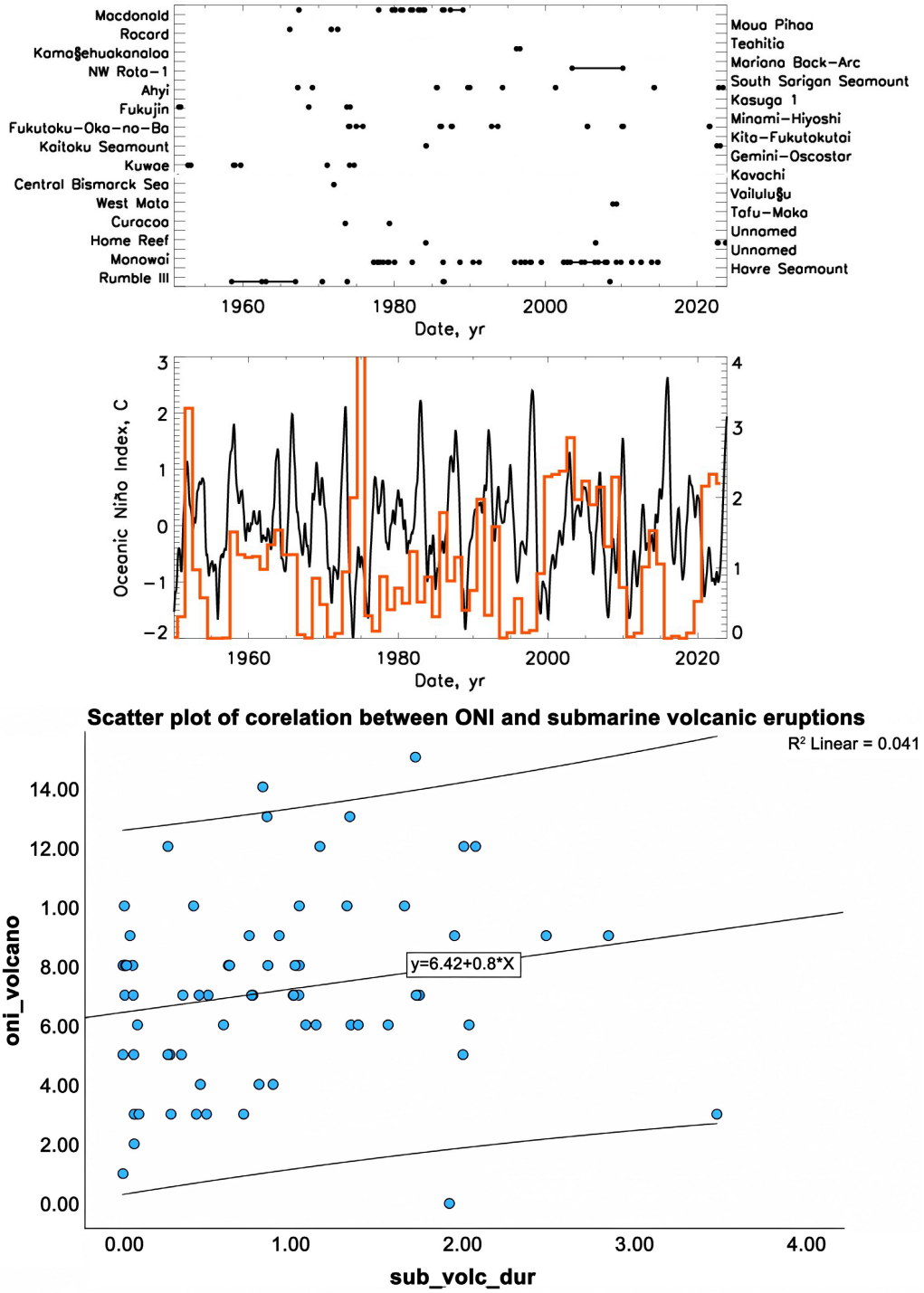

Figure 11. Top plot: The frequencies of underwater (submarine) volcanic eruptions including their power and duration. Middle plot: Temporal variations of frequencies of underwater volcanic eruptions (red curve) and ONI/EENSO index (black curve) Bottom plot: Scatter plot of correlation of the ONI index with the frequency of underwater volcanic eruptions in the ONI areas, correlation coefficient r = 0.25.

We explored 137 under-water volcanic eruptions with 29 volcanos with the 0 < VEI < 4 located in the ENSO occurrence areas as shown In **Figure 11** during the period of 1950 to 2023 years [77]. Maximal volcanic index VEI = 4 was for the eruption of volcano Home Reef which lasted from 13.08.2021 till 12.09.2021 (31 days). The dates and duration of eruptions of the submarine (underwater) volcanos with their names are shown in **Figure 11**, top plot. For more accurate consideration of the under-water volcanic eruptions on the ocean temperature we also considered the power of volcanic eruptions and their durations [77].

If we assume that the thermal energy deposited during a volcanic eruption is increased twice in the VEI increased by one and taking into account the duration of each eruption during a year. Then by summating the energy deposited by each volcano which had eruptions during the given year we calculate the energy deposited in this year by volcanic eruptions. The ONI index (black curve) and frequencies of the underwater volcanic eruptions (red curve) are presented in **Figure 11**, middle plot. The scatter plot of the correlation between the ONI index and frequency of the under-water volcanic eruptions [77] is shown in **Figure 11**, bottom plot.

It can be noted that that the correlation between ONI index and frequency of the underwater volcanic eruptions increased to 25%, becoming twice higher than the weaker correlation of 12% recorded between the ONI and the total number of volcanic eruptions (**Figure 10**, bottom plot, There is also an indication of a linear increase of the ONI index with the increase of the frequency of the under-water volcanic eruptions covering all the data within 95% confidence interval. This confirms rather significant involvements of the underwater volcanic eruptions in the formation of the ONI phenomena, in addition to any other local influences mentioned in the introduction.

3.3.3. Frequencies of Volcanic Eruptions versus a Distance of the Earth-Jupiter

The period of 12 years for ONI/ENSO variations derived from wavelet analysis in Section 3.3.1 indicates to a link with the Jupiter which has a period of 12 years for revolution about the Sun. The similar period of about 12 years was also reported for the seal levels in the two bays in Australia as demonstrated in Section 3.2. A comparison of the ONI index variation and Jupiter rotation curve curved shown in **Figure 11** in the paper by Zharkova and Vasilieva [77] revealed their similarity.

Now let us explore how the Earth-Jupiter distances are linked to the frequencies of volcanic eruptions, in general, and to those in the ONI/ENSO areas. The frequencies of all volcanic eruptions (blue line) and of ONI area volcanic eruptions (yellow line) versus the Earth-Jupiter distances are plotted in **Figure 12**. The mean eruption frequencies for both types of volcanic eruptions are shown by the solid lines of relevant colours and the standard deviation intervals are shown by the dashed lines of relevant colours.

It can be clearly seen in **Figure 12** that there are two specific distances from Earth to the planet of Jupiter where the numbers of volcanic eruptions are

exceeding significantly the mean numbers of eruptions. These distances are 4.5 au when Jupiter is closest to the Earth and of 6 au is when the Jupiter is further from the Earth but the Sun becoming closest to the Earth in its inertial motion while appearing on the same line between the Earth and Jupiter. In Figure 10 there is a scatter plot showing correlation of ONI/ENSO with the distance from the Earth to Jupiter with the correlation coefficient of 12%.

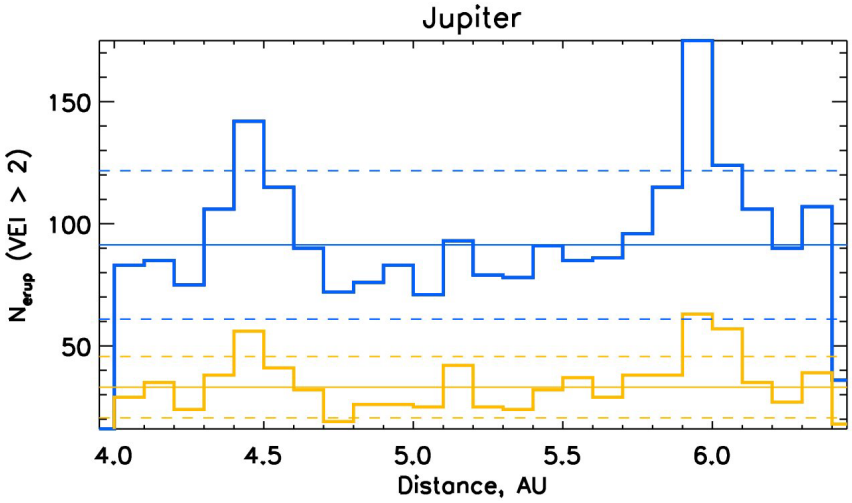

Figure 12. Dependence of frequencies of volcanic eruptions on the distances Earth-Jupiter taken from the NASA ephemeris Horizon for the whole Globe (blue line) and for the ONI/ENSO area (yellow line). The solid lines of each colour reproduces the average magnitudes and the dashed lines—standard deviation. Courtesy of Zharkova and Vasiljeva [77].

These increases of volcanic eruption numbers at distances 4.5 au and 6 au reveal that Jupiter have a dual effect on triggering volcanic eruptions by providing the important gravitational forcing on the Earth surface, in general and under water eruptions in two opposite positions when the Jupiter is closest to the Earth (4.5. au) and when the Sun is closest to Earth while Jupiter is located on the distance of 6 au while being on same line as Earth and Sun.

Either the gravity of Jupiter or of the Sun can trigger the tectonic processes which lead to volcanic eruptions on the surface or under water. The under-water volcanic eruptions, in turn, can significantly heat the ocean waters and lead to large increases of ONI/ENSO during the periods of 12 years occurring with the correlation of 25% as derived from the spectral analysis of ONI/ENSO in Section 2.1.

Let us now present in Figure 13 the scatter plot of the correlation of the volcanic eruptions in the ONI/ENSO area with the distances of Earth-Jupiter. It demonstrates a visible element (12%) of correlation of these two series that is confirmed statistically with Spearman correlation analysis carried with the IBM SPSS software. This correlation indicates that the gravitational forces of Jupiter can be a trigger some essential processes in the tectonic plates, which consequently cause

volcanic eruptions, thus, lending a support to the type of ONI/ENSO formation coming from the ocean advection discussed in introduction.

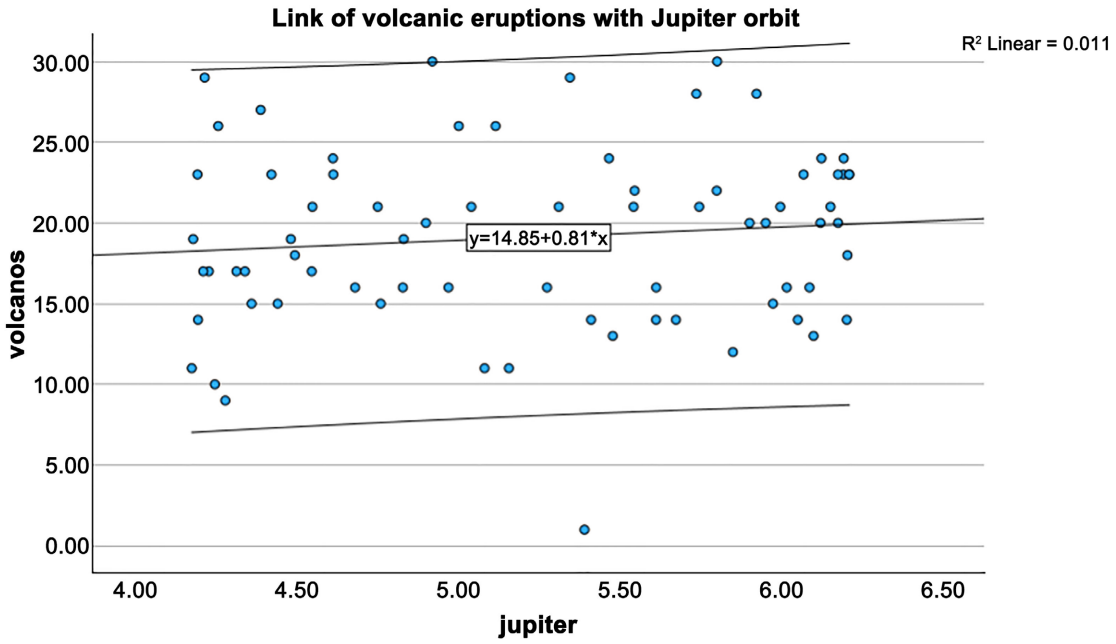

Figure 13. Scatter plot of the correlation (coefficient 0.12) of the frequency of volcanic eruptions in the ONI/ENSO area with the distance (au) between the Earth and Jupiter taken from the official Horizon ephemeris (NASA). The central line presents a linear fit of the data, the outer lines show 95% confidence interval of the fit.

3.3.4. Links of Volcanic Eruptions with the Periods of Moon Revolution

Periods of astronomically generated high tides contribute to the occurrence of extreme sea levels. There are two precessions associated with the orbit of the Moon which cause systematic variation of high tides. The influence of the 18.61 year lunar nodal cycle and the 8.85 year cycle of lunar perigee which affects high tidal levels as a quasi 4.4 year cycle on high tidal levels on a global scale were investigated by [76]. The detection of the occurrence of 4.5 years in the ENSO periodicity shown in Section 3.3.1 clearly indicates to the effect on ENSO of the lunar perigee cycle.

We explored 2234 volcanic eruptions and built the dependence of a frequency of volcanic eruptions as a function of the Moon's coordinates. For volcanos with the precise dates of eruption (after 1875) we plotted a dependence of the eruption frequencies on the position of the Moon using the website https://ssd.jpl.nasa.gov/horizons.

Now let us explore periods of the lunar motion with the volcanic eruptions in the ONI/EGSO areas. In **Figure 14** there are shown the wavelet of the detected periods of the moon revolution (left) and the wavelet of periods in frequencies of volcanic eruptions (right plot). It can be noted that the wavelet analysis of the moon periods reveals clearly the most prominent period of 27.8 days, then noticeable periods oof 203, and407 days and the period of 3262 (8.9 years) linked to the lunar semidiurnal period for a small node declination.

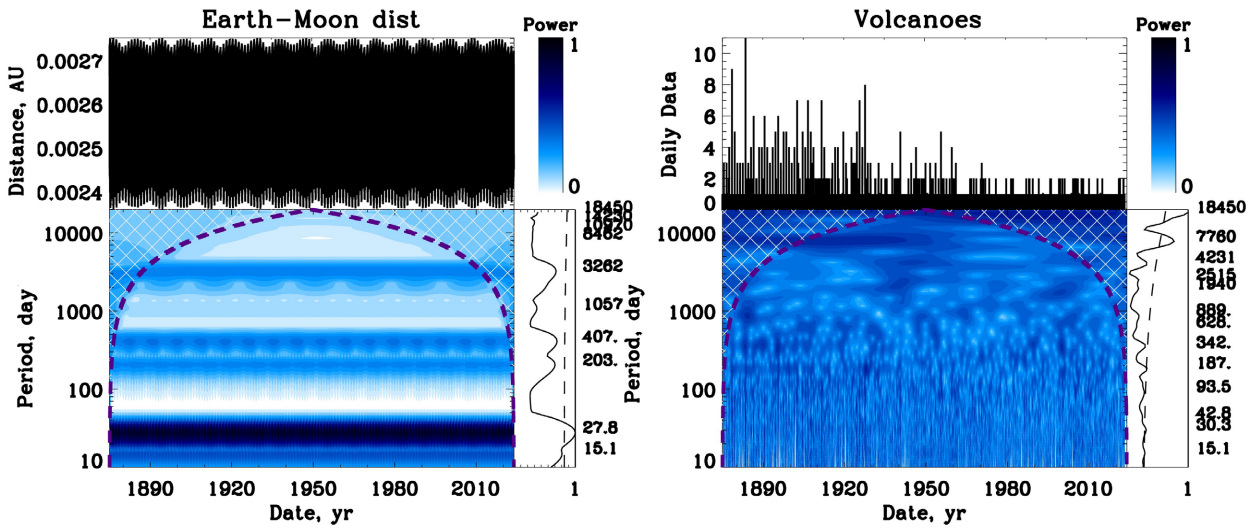

Figure 14. Left plot: Wavelet analysis of the Earth-Moon distances for 1875-2024 years. There is aa significant period of 27 days and some additional periods of 203, 407 and 3282 days (8.9 years) that is the lunar semidiurnal perigee period for small inclination. Right plot: Wavelet analysis of the frequencies of volcanic eruption with VEI > 2 for the same years. The periods in the wavelet spectra are marked in days. There is a significant period of 7760 days (21.3 years) detected.

This link indicates that it is very likely that the tidal forces of the moon caused by the precession of its orbit perigee can also cause additional volcanic eruptions, similar to these caused by Jupiter. The volcanic eruption frequencies show that besides the known link to summary curve variation of the eigen vectors of SBMF with a period of 21.3 years, there are noticeable period of eruptions associated with the Jupiter period of 12 years (4231 days) and the period close to 3262 days of the lunar perigee period of 8.9 years. This 8.9 year period is valid for the whole globe while for the southern hemisphere where ONI/ENSO operates it turns to be the 4.5 year period reported in Section 3.3.1.

In Figure 15, the frequencies of volcanic eruption are plotted as a function of the Right Accession (RA) (top left plot) and on a distance Earth-Moon (top right plot). Possible positions of the Moon from the minimal to maximal were divided by 24 equal intervals for RA and 18 equal intervals for distances. For each interval a number of volcanic eruptions was calculated which appear at that time when Moon was in that position. The frequency of volcanic eruptions is reflected by the colour scheme place on the left for the RA-Distance plot in the top left plot and on the right in the Distance, Declination for the top right plot.

The bottom plots in Figure 15 show the plots of frequency of volcanic eruptions as a function of Right Accession, RA, (left plot) and of the Earth-Moon distances (right plot). The thin horizontal line indicates the averaged frequency oof volcanic eruptions. The horizontal dashed lines show the standard deviation.

It can be noted that the larges numbers of volcanic eruptions happen at 13 - 14 hours of Right Accession and at the Earth-Moon distances of about 0.00248 au (the Moon is closest to the Earth) and of about 0.00268 au when the Moon is on the same line with the Sun, similar to the ones occurred for Jupiter as discussed in

Section 3.3.3. [77]. And similarly to the effect of the gravitation by Jupiter, its maxima effect ion volcanic eruptions s achieved when the Moon is further from the Earth being opposite to but on the same line as the Sun, causing the stronger gravitational effect by the Sun on the volcanic eruption frequencies. This would support the stronger correlation of the frequency of volcanic eruptions with the Sun-Earth distances in January when the Earth is closest to the Sun in its current SIM and turned to the Sun with the Pacific ocean areas in the Southern hemisphere shown in Section 3.3.5.

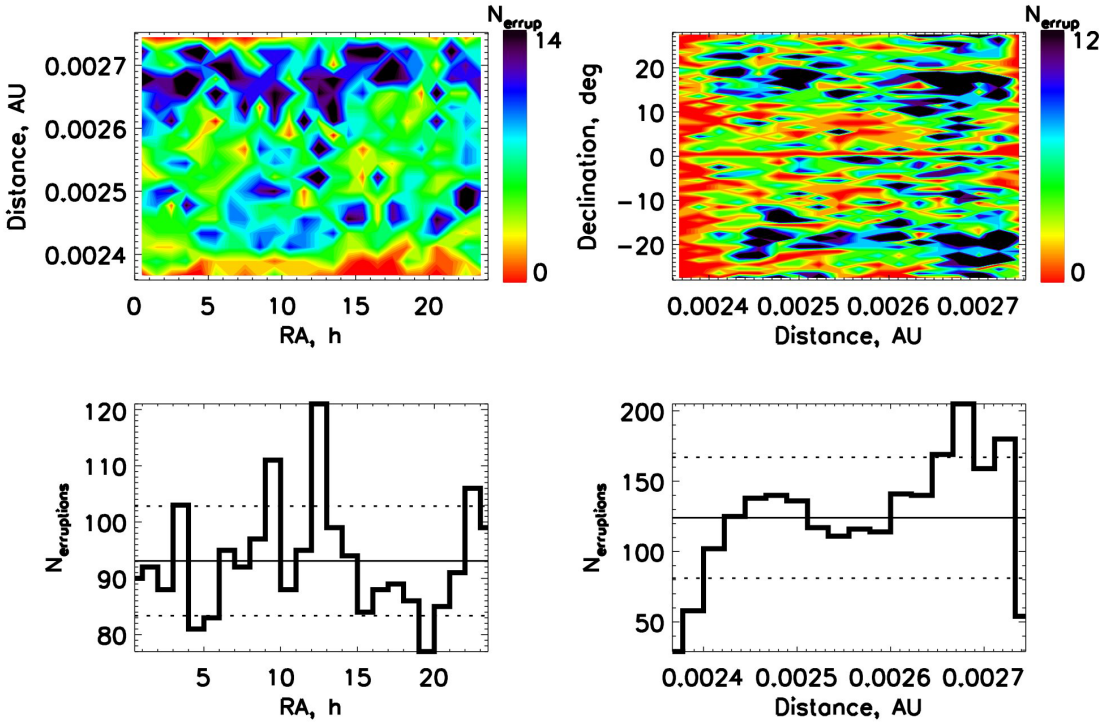

Figure 15. Top row: The frequencies of eruption as a function of the Right Accession (RA) (left plot) and of the Earth-Moon distance (right plot). The frequency of volcanic eruptions is reflected by the colour scheme placed on the right hand side. Bottom row: The integrated frequency of volcanic eruptions as function of RA (left plot) and of the Earth-Moon distances (right plot). Thin horizontal solid line indicates the averaged frequency oof volcanic eruptions, the horizontal dashed lines show the standard deviation magnitudes.

3.3.5. Links of ONI with January Distances of the Earth to the Sun

The effect of the solar system planet gravitation on the motion even of the star of the system, the Sun, leading to the solar inertial motion (SIM) about the barycentre of the solar system, has been reported by many authors [70] [71] [78] while only recently this effects has been linked to the changes in Sun-Earth distances on the orbit in different years, centuries or even millennia reporting the two-millennial variations pf solar irradiance (Hallstaat's cycle) caused by SIM [14] [15] [26]. In this millennium the Sun is shown to move closer tot the Earth orbit during passing the orbit about the spring equinox in the Northern hemisphere.

Based on the topology of SIM and the asymmetry of distances between the Sun and Earth in the summer and winter months, let us compare the ENSO index with

the distances between the Earth and Jupiter taken from the official Horizon ephemeris (NASA) measured on 15 January and 15 July of each year as discussed by [77].

It was noted that there is no noticeable correlation between the ONI/ENSO index and the Sun-Earth distances in July. This is fully understandable since for this connection the closest part to the Sun on Earth is the Northern hemisphere and not the Southern one where the ENSO occurs. However, there is much more significant connection is established between the ONI/ENSO index and the Sun-Earth distance in January (see **Figure 16**) possibly linked to the underwater volcanic eruptions discussed in Section 3.3.2.

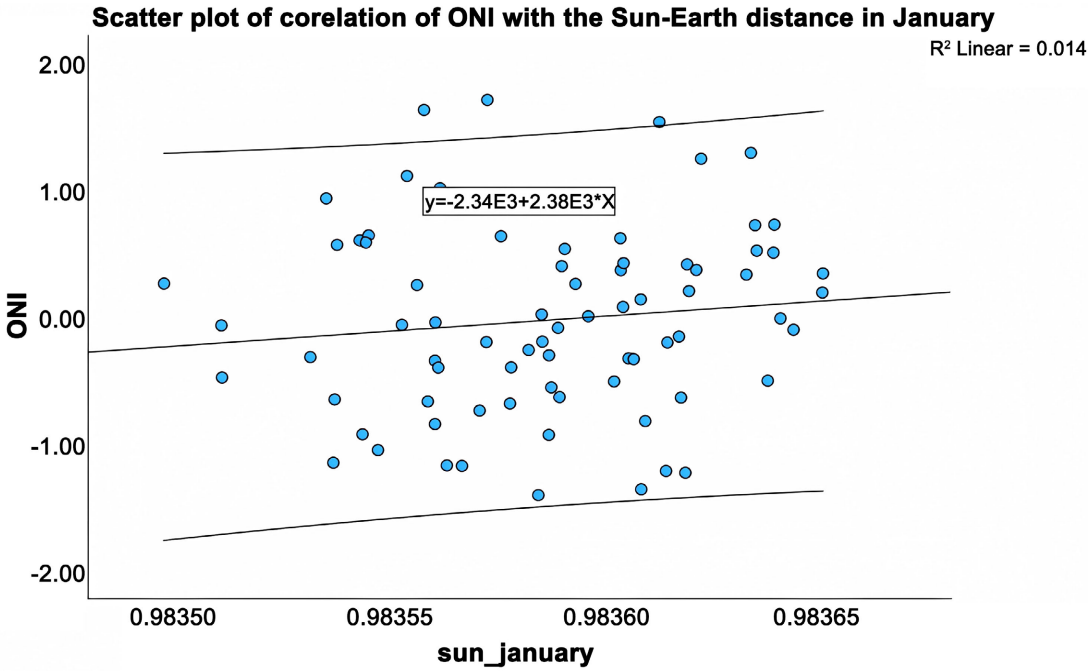

Figure 16. Scatter plot of the correlation (coefficient of 0.15) of the ONI/ENSO index with a distance (au) between the Earth and Sun taken from the official Horizon ephemeris (NASA) in January of each year shown in axis X. The central line presents a linear fit of the data, the outer lines show 95% confidence interval of the fit.

The scatter plot in **Figure 16** of correlation the ONI/ENSO index with a distance (au) between the Earth and Sun in January of each year taken from the official Horizon ephemeris (NASA) reveals the correlation coefficient of 15%. The central line presents a linear fit of the data, the outer lines show 95% confidence interval of the fit.

It can be seen that during the times of January of each years when the Earth is turned to the Sun with the southern hemisphere, where ONI/ENSO are formed, so the Sun-Earth distances are shortest, the correlation coefficient grow to 15% compared to 12% derived for the closest distance between the Earth and Jupiter. This indicates that the Sun's gravitation caused by the inertial motion induced by Jupiter and other large planets play a more important role than that by Jupiter itself, thus, initiating more volcanic eruptions, which are then lead to the

ONI/ENSO index increase.

4. Discussion and Conclusions

In this study we compare the links of the terrestrial temperature, the sea level, ice area in both hemispheres with a) the solar activity indices expressed through the averaged sunspot numbers and the summary curve of two largest eigen vectors of the solar background magnetic field and b) solar and planetary orbital motion imposed by the changes of the Earth-Jupiter, Earth-Moon and Sun-Earth distances caused by solar inertial motion imposed by the gravitation of large planets.

4.1. The Effects of Solar Activity

It was established that the sea level curve showed rather close similarity, in average, to the temporal variations of the temperature curves that was also reported by the other studies [45]-[50]. We aalso show from the wavelet analysis that the GLB dataset of terrestrial temperature and global sea level vary with a significant period of 21.4 years, which is clearly associated with the variations in solar activity defined by the summary curve of the largest eigen vectors of the SBMF [25] [26].

There is also a dominant 21.4-year period reported in the variations of the volcanic eruptions in the past 3 centuries corrrelaating with the summary curve of SBMF with the coefficient r = 84% [60]. At the same time, the Oceanic Niño Index (ONI) is found to have a strong (>87%) correlation with the Global Land-Ocean Temperature (GLOT). Although, it did not show any noticeable link (r = 1%) with the sunspot solar activity index.

It was shown that the weather patterns seem to affect the Northern and Southern hemispheres very differently. In the Northern hemisphere there were continuous variations of the ice areas occurring periodically with a period of 10.7 years that is a usual solar cycle defined by sunspots [25]. While Antarctica's ice areas do not reveal this link with the solar activity showing some periods of 5.6 and 15.6 years within the 95% confidence level, possibly, affected by some local features to be explored.

4.2. Orbital Motion Effects

On the other hand, the total solar irradiance (TSI) calculated from the Sun-Earth distances in March-August of every year of the last few centuries is found to grow with every year because the Sun moving closer to the Earth orbit owing to the gravitation of large planets (Jupiter, Saturn, Neptune and Uranus) called solar inertial motion (SIM). The SIM imposes a period of 2200-2300 years (Hallstatt's cycle) in TSI oscillations [26] which is detected in the Holocene data of solar irradiance measured from the abundance of ^{14}C isotope and confirmed with baseline variations of the SBMF. This increase of TSI is following closely the measured terrestrial temperature increase [26]. This measured TSI increase in the past 300 years is at variance with a constant TSI used by the IPCC as the current solar forcing.

Furthermore, the amount of TSI deposited on Earth in 2020 to the Northern

hemisphere between the spring and autumn equinox constitutes 50.103% of the overall TSI while between the autumn and spring equinox, or deposited to the Southern hemisphere,, constitutes 49.897% of the TSI for for the whole year. This means that during 2020 there was more than 0.2% TSI deposited to the Northern hemisphere then to the Southern one. Definitely, the solar forcing function used by IPCC has to be amended to reflect this deposition of solar energy during the spring-summer months, whose TSI follows closely the temperature variation measurements and the sea level curve linked to the temperature variations.

In addition, the wavelet analysis of ONI/ENSO revealed two significant periods of 4.5 and 12 years, linked to orbital motion of the Moon and Jupiter, respectively. It was also shown that there is a noticeable correlation of 25% of the ONI/ENSO index with the frequencies of the under-water (submarine) volcanic eruptions. These, in turn, are linked to the rotation of Jupiter, Moon and the solar inertial motion caused by the gravitation of Jupiter and other large planets which are likely act as triggers of large tectonic movements causing volcanic eruptions.

We show that the correlation of the frequency of under-water volcanic eruptions with the Jupiter-Earth distances approaches 12% while it increases to 15% for the Sun-Earth distances in January, when the Sun is closest to the Earth's Southern hemisphere where the ONI/ENSO occurs. This correlation lends a support to the mechanism of ONI/ENSO origin in the parts of Pacific ocean These can affect very significantly the exchange of CO_2 between the ocean and air following Henry's law that requires more detailed future investigation. These effects on ONI/ENSO are propagated to the whole planet via the interconnection of ENSO with many terrestrial events.

4.3. Conclusions

In summary, we have presented a piece of growing evidence that the terrestrial temperature, sea level and ice coverage variations on Earth are linked to the variations of solar activity and magnetic field, or its summary curve of the two largest eigenvectors reflecting the cycles of solar activity. The orbital motion of the Earth, Moon, and the Sun is caused by the gravitation of large planets in the solar system, which noticeably affects the sea level in the southern hemisphere and variations of the ONI/ENSO. Index also formed in the Pacific ocean under the effects of underwater volcanic eruptions.

The combined effects of the solar heating from the solar activity and orbital motion imposed by the variable Sun-Earth distances approach their maximum magnitudes during March-July of each year causing substantial heating of the Earth's atmosphere and sea that will keep increasing with every year of the current millennium (1600-2600) following the trajectory of solar inertial motion and magnetic polarity of the summary curve of the SBMF.

Acknowledgements

The authors express their deep gratitude to the anonymous referee for very useful

comments, from which the paper strongly benefited. The authors wish to express their many thanks to the NASA Goddard Institute of Space Science (GISS) (US) and the British meteorological Center in Hadley, for providing the temperature datasets, the Centre for protection of the environment of the USA and the Centre for Scientific and Industrial Research Organisation for providing the data of the sea level and the National Snow and Ice Data Center for providing the ice and snow data. The authors also express their deepest gratitude to the staff and directorate of Wilcox Solar Observatory, Stanford, US, for providing coherent long-term observations of full disk synoptic maps of the solar background magnetic field.

Author Contributions Statement

V.Z. formulated the problem, suggested the datasets to consider, and did calculations and analysis of the eigen vectors sbmf and TSI for different Sun-Earth distances and all the statistical analysis with SPSS. I.V. gathered and processed the temperature, ice area, sea level data and ONI index, analysed them with the wavelet tool, and plotted the graphs. V.Z. and I.V. compared and analysed the results, wrote and reviewed the manuscript.

Conflicts of Interest

The authors do not have any competing financial interests.

References

[1] Akasofu, S. (2010) On the Recovery from the Little Ice Age. *Natural Science*, **2**, 1211-1224. https://doi.org/10.4236/ns.2010.211149

[2] Hansen, J., Ruedy, R., Sato, M. and Lo, K. (2010) Global Surface Temperature Change. *Reviews of Geophysics*, **48**. https://doi.org/10.1029/2010rg000345

[3] Méndez-Vallejo, C., Simpson, N., Johnson, F. and Birt, A. (2023) Climate Change 2023: Synthesis Report (Full Volume) Contribution of Working Groups I, II and III to the Sixth Assessment Report of the Intergovernmental Panel on Climate Change. 10.59327/IPCC/AR6-9789291691647. https://www.researchgate.net/publication/372768149_Climate_Change_2023_Synthesis_Report_Full_Volume_Contribution_of_Working_Groups_I_II_and_III_to_the_Sixth_Assessment_Report_of_the_Intergovernmental_Panel_on_Climate_Change/citation/download

[4] Yim, S., Wang, B., Liu, J. and Wu, Z. (2013) A Comparison of Regional Monsoon Variability Using Monsoon Indices. *Climate Dynamics*, **43**, 1423-1437. https://doi.org/10.1007/s00382-013-1956-9

[5] Trenberth, K.E. and Hoar, T.J. (1997) El Niño and Climate Change. *Geophysical Research Letters*, **24**, 3057-3060. https://doi.org/10.1029/97gl03092

[6] Ashok, K., Guan, Z. and Yamagata, T. (2001) Impact of the Indian Ocean Dipole on the Relationship between the Indian Monsoon Rainfall and Enso. *Geophysical Research Letters*, **28**, 4499-4502. https://doi.org/10.1029/2001gl013294

[7] Ashok, K. and Yamagata, T. (2009) The El Niño with a Difference. *Nature*, **461**, 481-484. https://doi.org/10.1038/461481a

[8] Yeh, S., Kug, J., Dewitte, B., Kwon, M., Kirtman, B.P. and Jin, F. (2009) Erratum: El Niño in a Changing Climate. *Nature*, **462**, 674-674. https://doi.org/10.1038/nature08546

[9] Roy, I., Asikainen, T., Maliniemi, V. and Mursula, K. (2016) Comparing the Influence of Sunspot Activity and Geomagnetic Activity on Winter Surface Climate. *Journal of Atmospheric and Solar-Terrestrial Physics*, **149**, 167-179. https://doi.org/10.1016/j.jastp.2016.04.009

[10] Yu, J. and Kao, H. (2007) Decadal Changes of ENSO Persistence Barrier in SST and Ocean Heat Content Indices: 1958-2001. *Journal of Geophysical Research*: *Atmospheres*, **112**, D13106. https://doi.org/10.1029/2006jd007654

[11] Roy, I. (2018) Addressing on Abrupt Global Warming, Warming Trend Slowdown and Related Features in Recent Decades. *Frontiers in Earth Science*, **6**, Article No. 136. https://doi.org/10.3389/feart.2018.00136

[12] Kug, J., Jin, F. and An, S. (2009) Two Types of El Niño Events: Cold Tongue El Niño and Warm Pool El Niño. *Journal of Climate*, **22**, 1499-1515. https://doi.org/10.1175/2008jcli2624.1

[13] Yu, J. and Kim, S.T. (2010) Identification of Central-Pacific and Eastern-Pacific Types of ENSO in CMIP3 Models. *Geophysical Research Letters*, **37**, L15705. https://doi.org/10.1029/2010gl044082

[14] Zharkova, V.V., Shepherd, S.J., Zharkov, S.I. and Popova, E. (2019) Retracted Article: Oscillations of the Baseline of Solar Magnetic Field and Solar Irradiance on a Millennial Timescale. *Scientific Reports*, **9**, Article No. 9197. https://doi.org/10.1038/s41598-019-45584-3

[15] Zharkova, V. (2021) Millennial Oscillations of Solar Irradiance and Magnetic Field in 600-2600. In: Bevelacqua, J., Ed., *Solar System Planets and Exoplanets*, IntechOpen, 27-60. https://doi.org/10.5772/intechopen.96450

[16] SILSO World Data Center (2021) The International Sunspot Number. International Sunspot Number Monthly Bulletin and Online Catalogue.

[17] Zharkova, V.V., Shepherd, S.J., Popova, E. and Zharkov, S.I. (2015) Heartbeat of the Sun from Principal Component Analysis and Prediction of Solar Activity on a Millenium Timescale. *Scientific Reports*, **5**, Article No. 15689. https://doi.org/10.1038/srep15689

[18] Zharkova, V.V. and Shepherd, S.J. (2022) Eigenvectors of Solar Magnetic Field in Cycles 21-24 and Their Links to Solar Activity Indices. *Monthly Notices of the Royal Astronomical Society*, **512**, 5085-5099. https://doi.org/10.1093/mnras/stac781

[19] Zharkova, V.V., Vasilieva, I., Popova, E. and Shepherd, S.J. (2023) Comparison of Solar Activity Proxies: Eigenvectors versus Averaged Sunspot Numbers. *Monthly Notices of the Royal Astronomical Society*, **521**, 6247-6265. https://doi.org/10.1093/mnras/stad1001

[20] Eddy, J.A. (1976) The Maunder Minimum. *Science*, **192**, 1189-1202. https://doi.org/10.1126/science.192.4245.1189

[21] Zharkova, V. (2020) Modern Grand Solar Minimum Will Lead to Terrestrial Cooling. *Temperature*, **7**, 217-222. https://doi.org/10.1080/23328940.2020.1796243

[22] Lean, J., Beer, J. and Bradley, R. (1995) Reconstruction of Solar Irradiance since 1610: Implications for Climate Change. *Geophysical Research Letters*, **22**, 3195-3198. https://doi.org/10.1029/95gl03093

[23] Easterbrook, D.J. (2016) Evidence-Based Climate Science. Elsevier.

[24] Parker, D.E., Jones, P.D., Folland, C.K. and Bevan, A. (1994) Interdecadal Changes of

Surface Temperature since the Late Nineteenth Century. *Journal of Geophysical Research*: *Atmospheres*, **99**, 14373-14399. https://doi.org/10.1029/94jd00548

[25] Zharkova, V.V. and Vasilieva, I. (2023) Terrestrial Temperature, Sea Levels and Ice Area Links with Solar Activity and Solar Orbital Motion. *Natural Science*, **15**, 233-255.

[26] Zharkova, V.V., Vasilieva, I., Shepherd, S.J. and Popova, E. (2023) Periodicities of Solar Activity and Solar Radiation Derived from Observations and Their Links with the Terrestrial Environment. *Natural Science*, **15**, 111-147.

[27] Steinhilber, F., Beer, J. and Fröhlich, C. (2009) Total Solar Irradiance during the Holocene. *Geophysical Research Letters*, **36**, L19704. https://doi.org/10.1029/2009gl040142

[28] Steinhilber, F., Abreu, J.A., Beer, J., Brunner, I., Christl, M., Fischer, H., *et al.* (2012) 9,400 Years of Cosmic Radiation and Solar Activity from Ice Cores and Tree Rings. *Proceedings of the National Academy of Sciences of the United States of America*, **109**, 5967-5971. https://doi.org/10.1073/pnas.1118965109

[29] Roy, I. and Haigh, J.D. (2010) Solar Cycle Signals in Sea Level Pressure and Sea Surface Temperature. *Atmospheric Chemistry and Physics*, **10**, 3147-3153. https://doi.org/10.5194/acp-10-3147-2010

[30] Christoforou, P. and Hameed, S. (1997) Solar Cycle and the Pacific "Centers of Action". *Geophysical Research Letters*, **24**, 293-296. https://doi.org/10.1029/97gl00017

[31] van Loon, H. and Meehl, G.A. (2008) The Response in the Pacific to the Sun's Decadal Peaks and Contrasts to Cold Events in the Southern Oscillation. *Journal of Atmospheric and Solar-Terrestrial Physics*, **70**, 1046-1055. https://doi.org/10.1016/j.jastp.2008.01.009

[32] Ashok, K., Behera, S.K., Rao, S.A., Weng, H. and Yamagata, T. (2007) El Niño Modoki and Its Possible Teleconnection. *Journal of Geophysical Research*: *Oceans*, **112**, C11007. https://doi.org/10.1029/2006jc003798

[33] Chang, Y., Chen, M., Yokoyama, Y., Matsuzaki, H., Thompson, W.G., Kao, S., *et al.* (2009) Monsoon Hydrography and Productivity Changes in the East China Sea during the Past 100,000 Years: Okinawa Trough Evidence (MD012404). *Paleoceanography*, **24**, PA3208. https://doi.org/10.1029/2007pa001577

[34] Hao, T., Liu, X., Ogg, J., Liang, Z., Xiang, R., Zhang, X., *et al.* (2017) Intensified Episodes of East Asian Winter Monsoon during the Middle through Late Holocene Driven by North Atlantic Cooling Events: High-Resolution Lignin Records from the South Yellow Sea, China. *Earth and Planetary Science Letters*, **479**, 144-155. https://doi.org/10.1016/j.epsl.2017.09.031

[35] Moore, J.C., Grinsted, A., Zwinger, T. and Jevrejeva, S. (2013) Semiempirical and Process-Based Global Sea Level Projections. *Reviews of Geophysics*, **51**, 484-522. https://doi.org/10.1002/rog.20015

[36] Fyke, J., Sergienko, O., Löfverström, M., Price, S. and Lenaerts, J.T.M. (2018) An Overview of Interactions and Feedbacks between Ice Sheets and the Earth System. *Reviews of Geophysics*, **56**, 361-408. https://doi.org/10.1029/2018rg000600

[37] Turner, J., Orr, A., Gudmundsson, G.H., Jenkins, A., Bingham, R.G., Hillenbrand, C., *et al.* (2017) Atmosphere-Ocean-Ice Interactions in the Amundsen Sea Embayment, West Antarctica. *Reviews of Geophysics*, **55**, 235-276. https://doi.org/10.1002/2016rg000532

[38] Pritchard, H.D., Arthern, R.J., Vaughan, D.G. and Edwards, L.A. (2009) Extensive Dynamic Thinning on the Margins of the Greenland and Antarctic Ice Sheets. *Nature*,

461, 971-975. https://doi.org/10.1038/nature08471

[39] Rignot, E., Bamber, J.L., van den Broeke, M.R., Davis, C., Li, Y., van de Berg, W.J., *et al.* (2008) Recent Antarctic Ice Mass Loss from Radar Interferometry and Regional Climate Modelling. *Nature Geoscience*, **1**, 106-110. https://doi.org/10.1038/ngeo102

[40] Joughin, I., Smith, B.E. and Holland, D.M. (2010) Sensitivity of 21st Century Sea Level to Ocean-Induced Thinning of Pine Island Glacier, Antarctica. *Geophysical Research Letters*, **37**, L20502. https://doi.org/10.1029/2010gl044819

[41] Favier, L., Durand, G., Cornford, S.L., Gudmundsson, G.H., Gagliardini, O., Gillet-Chaulet, F., *et al.* (2014) Retreat of Pine Island Glacier Controlled by Marine Ice-Sheet Instability. *Nature Climate Change*, **4**, 117-121. https://doi.org/10.1038/nclimate2094

[42] Park, J.W., Gourmelen, N., Shepherd, A., Kim, S.W., Vaughan, D.G. and Wingham, D.J. (2013) Sustained Retreat of the Pine Island Glacier. *Geophysical Research Letters*, **40**, 2137-2142. https://doi.org/10.1002/grl.50379

[43] Wingham, D.J., Wallis, D.W. and Shepherd, A. (2009) Spatial and Temporal Evolution of Pine Island Glacier Thinning, 1995-2006. *Geophysical Research Letters*, **36**, L17501. https://doi.org/10.1029/2009gl039126

[44] Cazenave, A., Dieng, H., Meyssignac, B., von Schuckmann, K., Decharme, B. and Berthier, E. (2014) The Rate of Sea-Level Rise. *Nature Climate Change*, **4**, 358-361. https://doi.org/10.1038/nclimate2159

[45] Rahmstorf, S. (2007) A Semi-Empirical Approach to Projecting Future Sea-Level Rise. *Science*, **315**, 368-370. https://doi.org/10.1126/science.1135456

[46] Nerem, R.S., Beckley, B.D., Fasullo, J.T., Hamlington, B.D., Masters, D. and Mitchum, G.T. (2018) Climate-Change-Driven Accelerated Sea-Level Rise Detected in the Altimeter Era. *Proceedings of the National Academy of Sciences of the United States of America*, **115**, 2022-2025. https://doi.org/10.1073/pnas.1717312115

[47] Storch, H.V., Zorita, E. and González-Rouco, J.F. (2008) Relationship between Global Mean Sea-Level and Global Mean Temperature in a Climate Simulation of the Past Millennium. *Ocean Dynamics*, **58**, 227-236. https://doi.org/10.1007/s10236-008-0142-9

[48] Grinsted, A., Moore, J.C. and Jevrejeva, S. (2009) Reconstructing Sea Level from Paleo and Projected Temperatures 200 to 2100 AD. *Climate Dynamics*, **34**, 461-472. https://doi.org/10.1007/s00382-008-0507-2

[49] Vermeer, M. and Rahmstorf, S. (2009) From the Cover: Global Sea Level Linked to Global Temperature. *Proceedings of the National Academy of Sciences of the United States of America*, **106**, 21527-21532. https://doi.org/10.1073/pnas.0907765106

[50] Sannino, G., Carillo, A., Iacono, R., Napolitano, E., Palma, M., Pisacane, G., *et al.* (2022) Modelling Present and Future Climate in the Mediterranean Sea: A Focus on Sea-Level Change. *Climate Dynamics*, **59**, 357-391. https://doi.org/10.1007/s00382-021-06132-w

[51] Oman, L., Robock, A. and Stenchikov, G. (2003) Comparing the Climatic Impact from Low Latitude versus High Latitude Volcanic Eruptions. *AGU Fall Meeting Abstracts*, San Francisco, 8-12 December 2003.

[52] Emile-Geay, J., Seager, R., Cane, M.A., Cook, E.R. and Haug, G.H. (2008) Volcanoes and ENSO over the Past Millennium. *Journal of Climate*, **21**, 3134-3148. https://doi.org/10.1175/2007jcli1884.1

[53] Salby, M.L., Titova, E.A. and Deschamps, L. (2012) Changes of the Antarctic Ozone Hole: Controlling Mechanisms, Seasonal Predictability, and Evolution. *Journal of Geophysical Research: Atmospheres*, **117**, D10111.

https://doi.org/10.1029/2011jd016285

[54] Koutsoyiannis, D., Onof, C., Kundzewicz, Z.W. and Christofides, A. (2023) On Hens, Eggs, Temperatures and CO_2: Causal Links in Earth's Atmosphere. *Sci*, **5**, Article No. 35. https://doi.org/10.3390/sci5030035

[55] Torrence, C. and Compo, G.P. (1998) A Practical Guide to Wavelet Analysis. *Bulletin of the American Meteorological Society*, **79**, 61-78. https://doi.org/10.1175/1520-0477(1998)079<0061:apgtwa>2.0.co;2

[56] Lenssen, N.J.L., Schmidt, G.A., Hansen, J.E., Menne, M.J., Persin, A., Ruedy, R., *et al.* (2019) Improvements in the GISTEMP Uncertainty Model. *Journal of Geophysical Research*: *Atmospheres*, **124**, 6307-6326. https://doi.org/10.1029/2018jd029522

[57] Frederikse, T., Landerer, F., Caron, L., Adhikari, S., Parkes, D., Humphrey, V.W., *et al.* (2020) The Causes of Sea-Level Rise since 1900. *Nature*, **584**, 393-397. https://doi.org/10.1038/s41586-020-2591-3

[58] Church, J.A. and White, N.J. (2006) A 20th Century Acceleration in Global Sea-Level Rise. *Geophysical Research Letters*, **33**, L01602. https://doi.org/10.1029/2005gl024826

[59] Holgate, S.J. and Woodworth, P.L. (2004) Evidence for Enhanced Coastal Sea Level Rise during the 1990s. *Geophysical Research Letters*, **31**, L07305. https://doi.org/10.1029/2004gl019626

[60] Vasilieva, I. and Zharkova, V. (2023) Terrestrial Volcanic Eruptions and Their Association with Solar Activity. *Global Journal of Science Frontier Research*, **23**, 22-43.

[61] Velasco Herrera, V.M., Soon, W. and Legates, D.R. (2021) Does Machine Learning Reconstruct Missing Sunspots and Forecast a New Solar Minimum? *Advances in Space Research*, **68**, 1485-1501. https://doi.org/10.1016/j.asr.2021.03.023

[62] Le Mouël, J.L., Lopes, F. and Courtillot, V. (2020) Characteristic Time Scales of Decadal to Centennial Changes in Global Surface Temperatures over the Past 150 Years. *Earth and Space Science*, **7**, e00671. https://doi.org/10.1029/2019ea000671

[63] Stothers, R.B. (1989) Volcanic Eruptions and Solar Activity. *Journal of Geophysical Research*: *Solid Earth*, **94**, 17371-17381. https://doi.org/10.1029/jb094ib12p17371

[64] Maezawa, K. (1974) Dependence of the Magnetopause Position on the Southward Interplanetary Magnetic Field. *Planetary and Space Science*, **22**, 1443-1453. https://doi.org/10.1016/0032-0633(74)90040-3

[65] Perreault, P. and Akasofu, S. (1978) A Study of Geomagnetic Storms. *Geophysical Journal International*, **54**, 547-573. https://doi.org/10.1111/j.1365-246x.1978.tb05494.x

[66] Stauning, P. (1994) Coupling of IMF b_y Variations into the Polar Ionospheres through Interplanetary Field-Aligned Currents. *Journal of Geophysical Research*: *Space Physics*, **99**, 17309-17322. https://doi.org/10.1029/94ja00927

[67] Stauning, P., Clauer, C.R., Rosenberg, T.J., Friis-Christensen, E. and Sitar, R. (1995) Observations of Solar-Wind-Driven Progression of Interplanetary Magnetic Field B_y-Related Dayside Ionospheric Disturbances. *Journal of Geophysical Research*: *Space Physics*, **100**, 7567-7585. https://doi.org/10.1029/94ja01825

[68] Gonzalez, W.D., Tsurutani, B.T. and Clúa de Gonzalez, A.L. (1999) Interplanetary Origin of Geomagnetic Storms. *Space Science Reviews*, **88**, 529-562. https://doi.org/10.1023/a:1005160129098

[69] Prosovetsky, D.V. and Myagkova, I.N. (2011) The Correlation between Geomagnetic Disturbances and Topology of Quasi-Open Structures in the Solar Magnetic Field.

Geomagnetism and Aeronomy, **51**, 1078-1082.
https://doi.org/10.1134/s0016793211080342

[70] Charvátová, I. (2000) Can Origin of the 2400-Year Cycle of Solar Activity Be Caused by Solar Inertial Motion? *Annales Geophysicae*, **18**, 399-405.
https://doi.org/10.1007/s005850050897

[71] Paluš, M., Kurths, J., Schwarz, U., Seehafer, N., Novotná, D. and Charvátová, I. (2007) The Solar Activity Cycle Is Weakly Synchronized with the Solar Inertial Motion. *Physics Letters A*, **365**, 421-428. https://doi.org/10.1016/j.physleta.2007.01.039

[72] Perminov, A.S. and Kuznetsov, E.D. (2018) Orbital Evolution of the Sun-Jupiter-Saturn-Uranus-Neptune Four-Planet System on Long-Time Scales. *Solar System Research*, **52**, 241-259. https://doi.org/10.1134/s0038094618010070

[73] Connolly, R., Soon, W., Connolly, M., Baliunas, S., Berglund, J., Butler, C.J., *et al.* (2023) Challenges in the Detection and Attribution of Northern Hemisphere Surface Temperature Trends since 1850. *Research in Astronomy and Astrophysics*, **23**, Article ID: 105015. https://doi.org/10.1088/1674-4527/acf18e

[74] Soon, W., Connolly, R., Connolly, M., Akasofu, S., Baliunas, S., Berglund, J., *et al.* (2023) The Detection and Attribution of Northern Hemisphere Land Surface Warming (1850-2018) in Terms of Human and Natural Factors: Challenges of Inadequate Data. *Climate*, **11**, Article No. 179. https://doi.org/10.3390/cli11090179

[75] van Westen, R.M., Kliphuis, M. and Dijkstra, H.A. (2024) Physics-Based Early Warning Signal Shows That AMOC Is on Tipping Course. *Science Advances*, **10**, eadk1189.
https://doi.org/10.1126/sciadv.adk1189

[76] Haigh, I.D., Eliot, M. and Pattiaratchi, C. (2011) Global Influences of the 18.61 Year Nodal Cycle and 8.85 Year Cycle of Lunar Perigee on High Tidal Levels. *Journal of Geophysical Research*, **116**, C06025. https://doi.org/10.1029/2010jc006645

[77] Zharkova, V.V. and Vasilieva, I. (2024) ENSO Index Variations and Links with Solar and Volcanic Activity. *Natural Science*, **16**, 25-44.
https://doi.org/10.4236/ns.2024.164004

[78] Charvatova, I. (1988) The Solar Motion and the Variability of Solar Activity. *Advances in Space Research*, **8**, 147-150. https://doi.org/10.1016/0273-1177(88)90184-6